

Award Number: W81XWH-11-1-0232

TITLE: Feasibility of Prostate Cancer Diagnosis by Transrectal Photoacoustic Imaging

PRINCIPAL INVESTIGATOR: Dr. Hanli Liu

CONTRACTING ORGANIZATION: University of Texas at Arlington  
Arlington, TX 76019

REPORT DATE: May 2014

TYPE OF REPORT: Final

PREPARED FOR: U.S. Army Medical Research and Materiel Command  
Fort Detrick, Maryland 21702-5012

DISTRIBUTION STATEMENT: Approved for Public Release;  
Distribution Unlimited

The views, opinions and/or findings contained in this report are those of the author(s) and should not be construed as an official Department of the Army position, policy or decision unless so designated by other documentation.

# REPORT DOCUMENTATION PAGE

Form Approved  
OMB No. 0704-0188

Public reporting burden for this collection of information is estimated to average 1 hour per response, including the time for reviewing instructions, searching existing data sources, gathering and maintaining the data needed, and completing and reviewing this collection of information. Send comments regarding this burden estimate or any other aspect of this collection of information, including suggestions for reducing this burden to Department of Defense, Washington Headquarters Services, Directorate for Information Operations and Reports (0704-0188), 1215 Jefferson Davis Highway, Suite 1204, Arlington, VA 22202-4302. Respondents should be aware that notwithstanding any other provision of law, no person shall be subject to any penalty for failing to comply with a collection of information if it does not display a currently valid OMB control number. **PLEASE DO NOT RETURN YOUR FORM TO THE ABOVE ADDRESS.**

|  |                    |                                       |   |                            |
|--|--------------------|---------------------------------------|---|----------------------------|
| <b>1. REPORT DATE (DD-MM-YYYY)</b><br>Rá ]ÁG€FH  |                    | <b>2. REPORT TYPE</b><br>Final report | <b>3. DATES COVERED (From - To)</b><br>FÁRáãÁG€FFÁĒÁGĪÁÔæãÁG€FH |                            |
| <b>4. TITLE AND SUBTITLE</b><br><br>Feasibility of Prostate Cancer Diagnosis<br>byÁTransrectal Photoacoustic Imaging   |                    |                                       | <b>5a. CONTRACT NUMBER</b>                                      |                            |
|  |                    |                                       | <b>5b. GRANT NUMBER</b><br>K , %Á K <!%Á%\$&' &                 |                            |
|  |                    |                                       | <b>5c. PROGRAM ELEMENT NUMBER</b>                               |                            |
| <b>6. AUTHOR(S)</b><br><br>F t0Hanli Liu, Ph.D<br><br>go ckrĵ cprkB wcŕf w   |                    |                                       | <b>5d. PROJECT NUMBER</b>                                       |                            |
|  |                    |                                       | <b>5e. TASK NUMBER</b>  |                            |
|  |                    |                                       | <b>5f. WORK UNIT NUMBER</b>                                     |                            |
| <b>7. PERFORMING ORGANIZATION NAME(S) AND ADDRESS(ES)</b><br><br>University of Texas at Arlington<br><br>Arlington, TX 76019   |                    |                                       | <b>8. PERFORMING ORGANIZATION REPORT NUMBER</b>                 |                            |
| <b>9. SPONSORING / MONITORING AGENCY NAME(S) AND ADDRESS(ES)</b><br>U.S. Army Medical Research and Materiel Command<br>Fort Detrick, Maryland 21702-5012   |                    |                                       | <b>10. SPONSOR/MONITOR'S ACRONYM(S)</b>                         |                            |
|  |                    |                                       | <b>11. SPONSOR/MONITOR'S REPORT NUMBER(S)</b>                   |                            |
| <b>12. DISTRIBUTION / AVAILABILITY STATEMENT</b><br><br>Approved for public release; distribution unlimited  |                    |                                       |   |                            |
| <b>13. SUPPLEMENTARY NOTES</b>   |                    |                                       |   |                            |
| <b>14. ABSTRACT</b><br><br>There is no effective imaging tool currently available for prostate cancer detection; needle biopsy is the current practice for diagnosis of the disease, aiming randomly in the prostate. Transrectal ultrasound has been used as a guiding tool to direct tissue needle biopsy for prostate cancer diagnosis; it cannot be utilized for detecting prostate cancer due to lack of sensitivity. Recent studies show that the combination of light and ultrasound may lead to a new imaging device that can be used to provide cancer-sensitive, ultrasound images for prostate cancer detection.<br><br>The goal of this study is to examine a new idea that combination of light and sound can lead to a better medical device so that doctors can clearly "see" harmful cancerous areas in the human prostate. The scientific basis for this idea is that when an organ is illuminated with light, cancer tissue will absorb more light and generate some heat. The light-generated heat, in turn, will be converted to sound wave and be "heard" by sound detectors. The cancerous sound waves will be plotted into images, allowing doctors "see" cancer better in the human prostate. The plan for the study includes two steps: (1) to setup the device and perform laboratory experiments using non-tissue samples, and (2) to calculate the measured data and thus to prove the new idea. |                    |                                       |   |                            |
| <b>15. SUBJECT TERMS</b><br>Technology Development, optical spectroscopy, transrectal probe, optical biopsy, auto-fluorescence spectroscopy, fluorescence life-time measurement.   |                    |                                       |   |                            |
| <b>16. SECURITY CLASSIFICATION OF:</b>   |                    |                                       | <b>17. LIMITATION OF ABSTRACT</b>                               | <b>18. NUMBER OF PAGES</b> |
| <b>a. REPORT</b>   | <b>b. ABSTRACT</b> | <b>c. THIS PAGE</b>                   |   |                            |
| ÁÁÁŪ   | Á Ū<br>ÁÁÁÁÁ       | Ū                                     | ŪŪ  | 41                         |
|  |                    |                                       | <b>19a. NAME OF RESPONSIBLE PERSON</b><br>ŪUNRĒRO               |                            |
|  |                    |                                       | <b>19b. TELEPHONE NUMBER (include area code)</b>                |                            |

## Table of Contents

|  |    |
|--|----|
| SF 298.....  | 1  |
| Table of Contents .....  | 2  |
| 1. Introduction.....   | 3  |
| 2. Body of the Report .....  | 3  |
| 2.1 <i>Development and investigation for Aim 1</i> .....   | 3  |
| 2.2 <i>Development and investigation for modified Aim 2</i> .....  | 8  |
| 2.3 <i>Optical properties of human prostate specimens quantified<br/>        by ex vivo measurements</i> ..... | 13 |
| 3. Key Research Accomplishments<br>and Reportable Outcomes .....   | 14 |
| 4. Conclusions .....   | 14 |
| 5. References.....   | 15 |
| 6. Published paper attached .....  | 16 |

**Appendix A:** Peter Leboulluec, Baohong Yuan, and **Hanli Liu**, “A compact and cost-efficient frequency-domain photoacoustic imaging technique,” *Am. J. of Phys.* Vol. 81, 712-717 (2013).

**Appendix B:** Vikrant Sharma, Ephrem O. Olweny, Payal Kapur, Jeffrey A. Cadeddu, Claus G. Roehrborn, and Hanli Liu, “Prostate cancer detection using combined auto-fluorescence and light reflectance spectroscopy: *ex vivo* study of human prostates,” *Biomedical Optics Express*, Vol. 5(5), 1512-1529 (2014).

# 2011-2014 Final Progress Report

This report presents the specific aims and accomplishments of our prostate cancer research project during the entire period of funding sponsored by the DoD Prostate Cancer Research Program. It covers our activities from April 1, 2011 to March 30, 2014.

## 1. Introduction

The goal of this study is to form the hypothesis that a transrectal photo-acoustic imaging (TR-PAI) device can be developed and will significantly enhance detection of aggressive cancerous areas in the human prostate.

### **The project has two specific aims:**

Aim 1: design and implement a laboratory-based TR-PAI system and perform laboratory experiments using tissue-blood phantoms;

Aim 2: Based on the laboratory phantom experiments, characterize the quality of reconstructed PAI, including image resolutions, position errors of the given simulated tumors, and quantification accuracy of the physiological parameters of simulated tumor tissues.

## 2. Body of the Report

### **2.1 Development and investigation for Aim 1**

Aim 1: design and implement a laboratory-based TR-PAI system and perform laboratory experiments using tissue-blood phantoms.

Photoacoustic (PA) imaging technologies have been investigated recently and are considered as a valuable and potentially powerful tool for both preclinical and clinical cancer imaging [1]. Currently, most PA imaging systems adopt a nanosecond pulsed laser with high pulse energy because a short light pulse can efficiently avoid energy loss due to thermal energy diffusion before the generation of PA signals, which is the so-called thermal confinement [2]. While the mainstream of PA research community is attempting to continuously improve the performance of PA technologies and explore various applications, another direction is significantly underdeveloped, which is how to develop a simple, compact and cost-efficient PA system for the use of widespread global health, including prostate cancer detection [3]. A nanosecond pulsed laser with high pulse energy is usually extremely expensive (from tens to hundreds of thousand dollars) and bulky (usually seats on a large optical table). This may not be a problem for a large research laboratory to conduct research projects. However, in many clinical cases due to costs and spaces, it is almost impossible to conduct PA imaging when using an expensive and bulky system. In contrast, a low cost and compact PA technique may be more useful and practical for research laboratories with limited resources, office-based clinics, and global healthcare in low- or middle-income countries. To significantly reduce the cost and size of a PA imaging system, in the first 1-1.5 years of funding, we developed a frequency-domain PA (FD-PA) system by using an inexpensive laser diode with a lock-in amplifier. This FD-PA technique is simple, compact and cost efficient but maintains decent performance compared with the expensive and bulky time-domain PA techniques. This FD-PA system is highly suitable for global health use, including prostate cancer detection.

In the following, we briefly report a simple frequency domain PA system and demonstrate its imaging capability. The corresponding theoretical derivations can be found in ref. [4] and/or Appendix A.

### 2.1.1 Measurement system

Figure 1 shows the experimental setup that was developed during the study. A function generator (FG, Agilent 33120A, Agilent Tech, CA) generates a sinusoidal voltage signal and a synchronized TTL signal with the same frequency ( $f$ ) and fixed phase shift. The sinusoidal signal is input into a homemade circuit to drive the laser diode (see figure 2 for details about the circuit). Thus, the laser intensity is modulated at the frequency of  $f$ . The laser diode has a central wavelength of 780 nm and a power of  $\sim 100$  mW when operating in DC mode (L785P100, Thorlabs). A lens is used to collimate the laser beam and a mechanical shutter is adapted for manually blocking the laser illumination to measure the background signal. At the same time, the synchronized TTL signal from the FG is input to a lock-in amplifier (LIA, SR844, Stanford Research Systems, CA) and used as a reference signal. The sample and the ultrasound transducer (UST, Olympus NDT, one inch in focal length) are submerged into a transparent tank that is filled with either water or Intralipid solution (an optical scattering medium). The sample is indocyanine green (ICG) aqueous solution which is injected into an optical and acoustic transparent tube (MRE-095, Braintree Scientific). The UST is focused on the sample. Both the lateral and axial sizes, (such as full width at half maximum—FWHM) of the focal zone depend on the central frequency of the UST. When the modulated laser reaches the optically absorbing sample, a PA wave is generated. The PA wave is picked up and converted into a voltage signal by the UST and further amplified (ZFL-1000LN, Mini Circuits) and filtered (SLP-5+, Mini Circuits). A total gain of 40 dB is applied by using two identical amplifiers in series that are driven by a DC power supply (BK Precision 1506). The processed PA signal is delivered to the LIA. The amplitude of the PA signal ( $V_{S0}$ ) and the phase difference between the PA signal and the reference signal ( $\Delta\theta$ ) are displayed on the screen of the LIA.

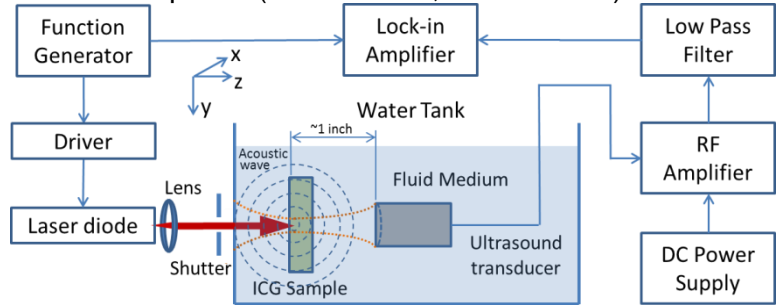


Figure 1: Experimental setup. The tank is filled with a liquid medium (either water or Intralipid solution).

Figure 2 shows the principle of the modulation circuit. The principle is straightforward. The FG serves as a DC and AC power source, which means output of the FG is an AC signal with certain DC offset. A resistor ( $R1$ ) and a potentiometer are used to limit and control the current flowing into the laser diode, respectively. The laser diode has a typical threshold current of 35 mA. The DC offset of the FG is  $V_{DC} = 2$  v and the AC peak-to-peak is  $V_{AC} = 4$  v. The total resistance of  $R1$  and the potentiometer is  $\sim 11$  ohms. A photodiode (EOT, ET-2030A) is used to verify the modulation of the laser intensity via an oscilloscope (2530B Digital Storage Oscilloscope, BK Precision)).

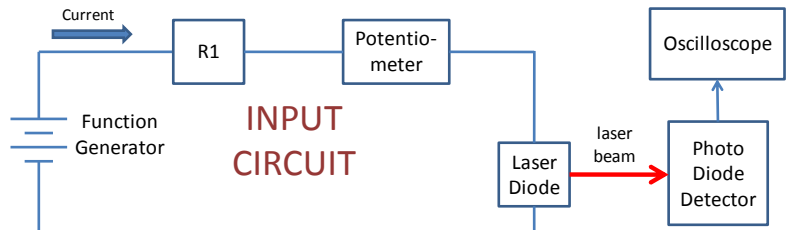


Figure 2: Principle of modulation circuit.

### 2.1.2 Data processing

Theoretically, the amplitude of the PA signal ( $V_{S0}$ ) alone can be used to extract or represent the optical absorption coefficient ( $\mu_a$ ), if other parameters in equations (3)-(5) given in Appendix A are known or can be estimated via other ways. However, in practice, it is common that the LIA shows a background signal even when the laser is turned off or blocked. This background signal is mainly caused by electronic interference from driving signal generated by the FG. Certainly,

carefully shielding the system and selecting specially designed cables may be helpful to reduce this interference. However, this will require more efforts and may significantly increase the system cost. Fortunately, this background interference is independent of the location of the UST or the sample. Therefore, a simple way to eliminate its effect is mathematically subtract it from the measured PA signal. Readers can obtain more details from Appendix A for this step.

### 2.1.3 Experiment results

#### Laser modulation results

Figure 3(a) shows the variation of the average power of the laser diode, modulated at 1 MHz, as a function of time. Note that the laser is attenuated to avoid possible damage of the power meter (PM100D, Thorlabs), which is used to detect the laser intensity. It can be seen that there is only a 0.2% drop in intensity over 80 minutes, thus the intensity is mostly steady. Similar results were found when changing the modulation frequency from 1 MHz to 2.25 MHz or changing the modulation from a sinusoidal wave to a square wave. Figure 3(b) shows the modulation strength (peak-to-peak voltage of the AC signal, see Fig.2 for the measurement method) as a function of the modulation frequency. The frequency was varied from 1 kHz to 15 MHz. The modulation intensity decreases slightly from 50 kHz to 15 MHz. Therefore, modulating

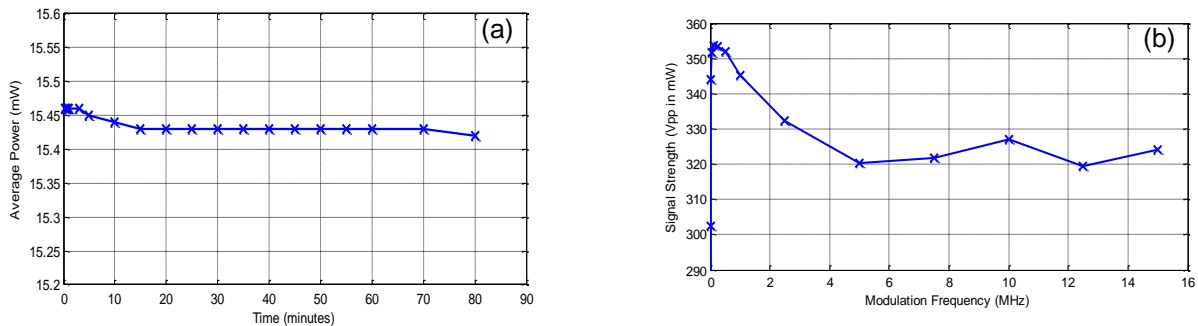


Figure 3(a) Measured average power of the laser diode as a function of the time. The power is stable over 80 minutes; 3(b) Laser diode signal strength as a function of the modulation frequency.

the laser diode at the UST frequencies of 1 MHz and 2.25 MHz is relatively stable.

#### Measurement of UST focal zone

To quantify the focal size of the UST, a similar technique as in Ref. [5] was adopted. Briefly, a pulser-and-receiver (5073PR Pulser/receiver, Olympus) is used to excite the UST and receive the reflected ultrasound signal. A metal wire with a small diameter (0.25 mm) is used as a sound reflector. By scanning the wire laterally and axially, the amplitude of the reflected ultrasound signal is recorded and displayed at each location. Figure 4 shows a typical result that represents a 2D ultrasound intensity distribution in the focal zone of a UST (2.25 MHz, NA=0.37). The color is proportional to the acoustic intensity. The lateral and axial FWHMs are  $\sim 0.72$  mm and  $\sim 6.8$  mm, respectively. Other transducers with different central frequencies have similar distribution patterns, but with different lateral and axial FWHMs. According to the principle of reciprocity, ultrasound transmission and detection of the same acoustic lens are reciprocal [6]. Therefore, the sensitivity area of detecting PA signal is considered the same as shown in figure 4.

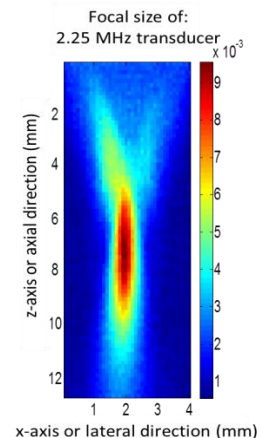


Figure 4

#### Photoacoustic measurements and imaging

To simulate biological tissue, the tank was filled with 1% intralipid solution (absorption and scattering coefficients of  $0.04 \text{ cm}^{-1}$  and  $8.4 \text{ cm}^{-1}$ , respectively, measured with an ISS Oximeter). An optically and acoustically transparent tube was filled with indocyanine green (ICG) aqueous solution, at a concentration of 0.5 grams/liter, to simulate an absorbing target for generating photoacoustic signals. The tube, which has an inner and outer diameter of 1.7 mm and 2.4 mm, respectively, was positioned along the y direction.

Figure 5 shows the measured photoacoustic signal ( $V_{PA}$ ) as a function of the horizontal or lateral position of the tube (along the x direction). One ultrasound transducer has a central frequency of 1 MHz and the FWHM of its lateral focal zone is about 1.3 mm. The narrow and wide rectangles represent the inner and outer diameter of the tube (1.7 mm and 2.4 mm), respectively. Clearly, the PA signals rise when the UST and laser beam gradually move into the tube region and fall when the UST and laser beam move away from the tube region. This result indicates that the highly absorbing ICG tube generates significant PA signals compared to the surrounding intralipid solution that has much lower absorption coefficient. This is because the absorption coefficient ( $\mu_a$ ) is proportional to PA signal strength. The FWHM of the PA data using the 1 MHz UST in Fig. 5 is about 2.3 mm. It is larger than the tube inner diameter (1.7 mm) and the UST lateral size (1.3 mm), which can be understood that the FWHM is mainly determined by the convolution between the profile of the tube cross section and the profile of the UST lateral focal zone.

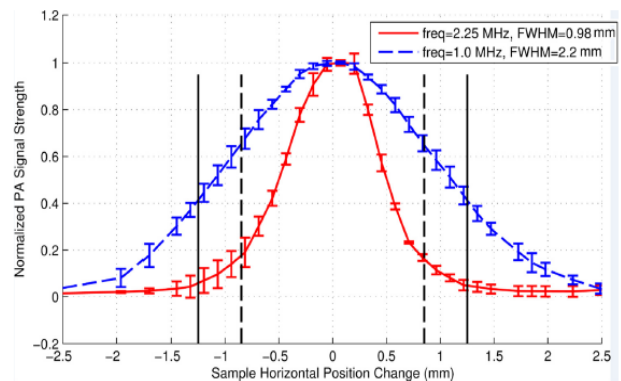


Figure 5: Normalized PA signal strength as a function of the sample horizontal location acquired from a 1 and 2.25 MHz UST. The tube is indicated by the vertical lines.

When increasing the frequency of the UST from 1 to 2.25 MHz, the FWHM of the UST's lateral focal zone reduces from  $\sim 1.3$  to  $\sim 0.72$  mm. Therefore, the PA spatial resolution can be improved when using a higher frequency UST. Figure 5 illustrates this point by showing that the FWHM of the PA signal measured from the 2.25 MHz UST is 0.96 mm which is smaller than that of the PA signal measured by the 1 MHz UST (2.3 mm). However, it is also smaller than the tube size and the reason is unknown.

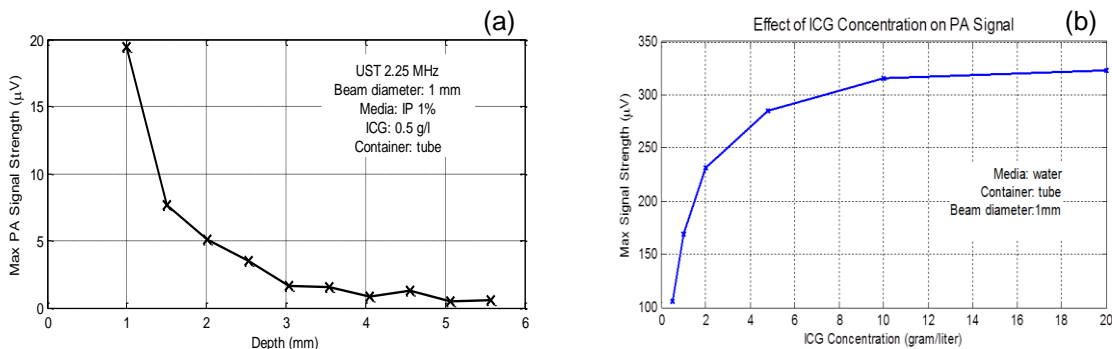


Figure 6 (a) Maximum PA signal strength as a function of depth. (b) Effect of ICG concentration on PA signal.

When increasing the tube depth (from the tank wall to the surface of the tube), the PA signal strength also decreases with increasing depth as shown in Fig. 6(a). This is due to the light

intensity  $I_0$  which significantly reduces when depth increases because of the light scattering. Furthermore, increasing ICG concentration leads to an increase in absorption coefficient of the tube ( $\mu_a$ ), which further raises the PA signal strength. Figure 6(b) shows the peak strength of the PA signal as a function of the ICG concentration. Clearly, the PA signal increases almost linearly when the concentration is low. However, the increase of the PA signal seems saturated at high concentration. This may be due to the fact that the light cannot penetrate into the high concentration ICG solution due to the large absorption coefficient of the high concentration ICG solution (that means that light absorption is limited at the superficial layer of the ICG solution).

Figures 7(a) and 7(b) show 2-dimensional (2D) images of the tube on x-y plane (C-mode, see the coordinates in Fig.1). They were acquired from a co-registered ultrasound and PA imaging system, respectively. Briefly, the PA system is same as the one described in Fig. 1. The pure ultrasound system has the same UST as the PA system. The UST was connected with a pulse-generator-receiver (5073PR Pulser/receiver, Olympus). The reflected ultrasound data was acquired by an oscilloscope (2530B Digital Storage Oscilloscope, BK Precision). Figure 7(c) shows the ultrasound image of the cross-section of the tube (B-mode, x-z plane). The two bright areas show the two boundaries of the tube. Note that the inner boundaries of the tube cannot be resolved from this image due to the limit resolution of the used UST (2.25 MHz). The dotted horizontal line indicates the depth of the C-mode image shown in Fig.7(a). Clearly, the ultrasound image shows the boundaries between the tube and the surrounding medium. The FWHM is about 1.5 mm in Fig. 7(a), which is comparable with the size of the tube. Figure 7(b) shows the corresponding PA image in the x-y plane. The image clearly shows the tube with optical (absorption) contrast.

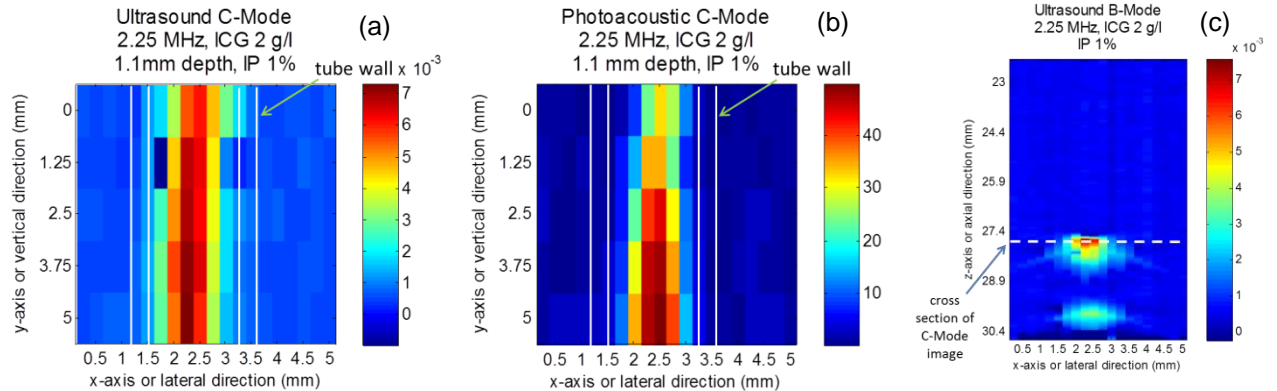


Figure 7 (a) A C-mode ultrasound image of the ICG filled tube. (b) A C-mode PA image of the same ICG filled tube. (c) An ultrasound B-mode image showing the cross section of the same ICG filled tube.

#### 2.1.4 Summary of research conducted for Aim 1

We have designed, implemented, and tested a frequency-domain photoacoustic imaging system using tissue-like phantoms. The imaging principle and data processing method have been presented and verified. The measured PA signal strength depends on the absorption coefficient, depth of the target, and the modulated light intensity of the laser diode. We have learned that appropriately processing the measured PA data and background interference is an important key to correctly display the PA images. The lateral spatial resolution of PA images is dependent on ultrasound frequencies and focal size of the ultrasound transducers. Although the current system has a low axial resolution (due to the adopted ultrasound transducer), the axial resolution can be significantly improved by using a high numerical aperture ultrasound transducer or by adopting a frequency-swept technique [7]. The FD-PA imaging system is cost efficient as compared with a time-domain imaging system.

In the meantime, however, we also learned that the frequency-domain photoacoustic imaging method developed by our approach has a severe limitation in sensing tissue signals deeper than 5 mm. Then, we tried to alter or modify our original idea by developing an integrated approach between ultrasound and optical tomography, namely, transrectal ultrasound-guided diffuse optical tomography (TRUS-DOT) for improved prostate cancer imaging. During the no-cost extension period, we have made great progress and obtained promising results using tissue-phantom experiments. In the following section, we provide details on this modified/updated approach with computer simulations and experimental results.

## **2.2 Development and investigation for modified Aim 2**

### **2.2.1 Hierarchical clustering to improve TRUS-DOT for prostate cancer imaging**

Diffuse optical tomography (DOT) is a non-invasive imaging modality, which utilizes near infrared (NIR) light and provides blood-based absorption maps within the detected tissue volume interrogated by the optical optodes. When using multiple wavelengths, DOT is also capable of measuring chromophore concentrations, such as oxy-hemoglobin, deoxy-hemoglobin, and water. Usage of DOT for breast cancer detection has been extensively studied. DOT instrumentation can be divided into three categories based on the principle of operation: (1) time resolved systems, (2) frequency domain systems and (3) continuous wave (CW) systems. Measurements in DOT can be made in the form of transmission, reflectance, or both. Time resolved systems rely on photon counting or gated imaging, which measures time of flight of photons through the tissue. However, these systems are very costly and bulky in comparison with CW systems. The frequency domain systems modulate the light source (e.g., laser diode) typically in the radio frequency range (e.g., 100 MHz) and measure the amplitude and phase shift of the detected signals. CW systems are the simplest, cost effective, and fastest in data collection; they can be made to image tissues at a video-rate. However, since CW systems measure only intensities of the reflected or transmitted light, they cannot separate the absorption and scattering effects of the tissue.

Despite of the instrumentation utilized, DOT has poor spatial resolution. Measurements in reflectance geometry are even worse in spatial resolution than in the transmission geometry. The cause that limits the spatial resolution of DOT is light scattering and diffusion in tissues, making DOT have to solve an underdetermined and ill-posed inverse problem. One way to improve the spatial resolution is to couple DOT techniques with other imaging techniques, such as MRI, ultrasound (US), and others. This process is usually done by combining a *priori* information in the inversion procedure. In particular, a combined usage of TRUS with DOT could improve the accuracy in identifying prostate cancer 1-2 centimeters below the prostate surface, as studied previously [8]. However, this reported approach treated each anatomical region, such as the rectum wall, prostate gland, and prostate cancer lesion, to be homogenous and thus to be reconstructed with uniform optical properties within each region. However, the reconstructed images by the reported method [8] could be erroneous because of the fact that TRUS does not provide a clear or clean signature for prostate cancer. On the other hand, it has been demonstrated that the spatial resolution of reconstructed DOT images depends upon the number and locations of optical sources and detectors utilized. Given the limited space available in TRUS, the idea to incorporate more sources and detectors for a combined TRUS-DOT approach seems not to be very practical.

To solve the problems given above, we made new development in two aspects: (1) development of hierarchical clustering method (HCM) for improved contrast recovery and spatial resolution in DOT for prostate cancer imaging; (2) development of Trans-rectal compatible

optical probe and instrumentation for prostate cancer imaging. First, in Section 2.2.2, we will explain the HCM procedure and demonstrate the capability of HCM using computer simulations. Then, in Section 2.2.3, we will explain the instrumentation utilized for trans-rectal compatible DOT and demonstrate the capability of HCM using laboratory phantoms.

## 2.2.2 Introduction, implementation, and Investigation of hierarchical clustering

### Principle and algorithm of HCM

In standard practice, the equation used to iteratively update DOT image reconstruction is given by [9,10]

$$(J^T J + 2\lambda I)(\delta\mu_a) = J^T (y - F(\mu_a)) \quad (1)$$

where  $J$  is the Jacobin matrix (or called sensitivity matrix),  $I$  is the identity matrix,  $\mathbf{y}$  is the measured data in a matrix form,  $\mathbf{F}$  is the operator that generates the forward model for light propagation in tissues,  $\mu_a$  is the vector of optical properties, and  $\lambda$  is the regularization parameter. Note that changes only in  $\mu_a$  are considered in eq. (1), because our DOT measurement utilizes CW NIR light with an assumption that variation in light scattering across the medium is minimal.

In our HCM method, we divide the region of interest (ROI) (i.e., the prostate region) into several geometric clusters. We assume that each of the geometric clusters/units is homogeneous and has the same optical property. In this way, the computational domain could be partially heterogeneous since the domain may contain several geometric units. Specifically, the nodes in the mesh are tagged and separated into subsets ( $GS_1, GS_2 \dots GS_i$ ) with respect to each unit. The Jacobian matrix in eq. (1) is then modified to  $J^*$  and is given by  $J^* = JS$ , where  $S$  matrix had a size of  $NN \times NS$ , where  $NN$  is the number of nodes within the specific unit/cluster and  $NS$  is the number of geometric clusters. The elements of  $S$  matrix are given by [10]:

$$S_{(i,j)} = \begin{cases} 1 & \text{if } i \in GS_i \\ 0 & \text{else} \end{cases} \quad (2)$$

At the end of each iteration, the solution vector is mapped back to each node using the following equation

$$\delta\mu_a = S(\delta\mu_a^*) \quad (3)$$

$\mu_a^*$  is a vector with optical properties of geometric clusters. When reconstructing two ROIs or clusters, such as background and anomaly, the background mesh was geometrically segmented in a heterogeneous fashion. For multiple clusters, we hierarchically implemented the proposed method by segmenting the region which is more prone to cancer, utilizing available prior spatial information. Specifically, we applied the proposed method in four steps, as shown in Fig. 8.

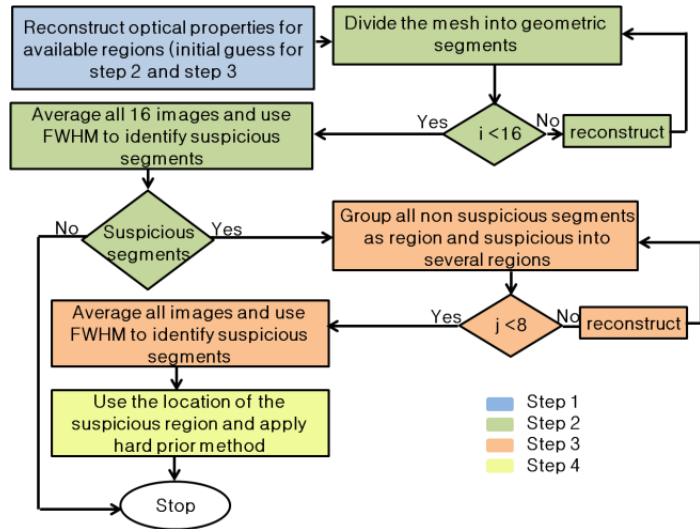


Figure 8: Flow chart indicating steps involved in HCM.

In step 1, the reconstruction is done based on TRUS images and the assumption of a homogeneous prostate. With such prior spatial information, the reconstructed  $\mu_a$  values in both background and prostate region should be reasonably accurate with respect to the actual values. Then, the reconstructed  $\mu_a$  values in available ROIs would serve as the initial guess in step 2 and step 3.

Step 2 of our method is dedicated to finding the probable locations of anomalies (i.e., prostate tumors). To achieve this, we geometrically divide the prostate region into several clusters, so the prostate tissue becomes a heterogeneous medium. However, without prior knowledge of suspicious locations, dividing the prostate into several clusters may result in mixing of suspicious tissue with normal prostate tissue and vice versa. In order to prevent this situation, we segment the prostate volume with different unit volume sizes iteratively. Specifically, we chose a unit volume as an initial segment size which is  $1 \times 1 \times 1 \text{ cm}^3$  in each of the  $x$ ,  $y$  and  $z$  dimensions. Then, we vary the volume size by increasing the linear length of the volume unit in each dimension iteratively. For example, an increase in length of 0.5 cm in only  $x$  direction gave rise to a unit volume of  $1.5 \times 1 \times 1 \text{ cm}^3$ , followed by the same length increase in only  $y$  or only  $z$  direction. In this way, we can generate 8 different unit volumes in three  $x$ ,  $y$ ,  $z$  directions, by increasing the linear length in only one dimension ( $x$ ,  $y$ ,  $z$ ), or in two dimensions ( $xy$ ,  $yz$ ,  $xz$ ), or in three dimensions ( $xyz$ ) and the initial size.

The procedure is given as follows (see Fig. 8): (1) reconstruct an initial  $\mu_a$  image with a starting base unit size (i.e.,  $1 \times 1 \times 1 \text{ cm}^3$ ), (2) save the reconstructed image, and go back and change the unit volume size (e.g.,  $1.5 \times 1 \times 1 \text{ cm}^3$  or  $1.5 \times 1.5 \times 1 \text{ cm}^3$  or  $1.5 \times 1.5 \times 1.5 \text{ cm}^3$ ) and reconstruct the image again (Step 2 in Fig. 8). To be more comprehensive, we next increase our base unit volume from  $1 \times 1 \times 1 \text{ cm}^3$  to  $1.5 \times 1.5 \times 1.5 \text{ cm}^3$  and then to  $2 \times 2 \times 2 \text{ cm}^3$ , with the same length interval of 0.5 cm applied to increase the base unit (e.g.,  $2 \times 1.5 \times 1.5 \text{ cm}^3$ ,  $2 \times 2 \times 1.5 \text{ cm}^3$ , or  $2 \times 2 \times 2 \text{ cm}^3$ ). In this way, we are able to generate another set of 8 reconstructed images with varied base unit volumes, resulting in an overall 16 ( $i=16$ ) images by the end of step two. (3) We average all of the reconstructed  $\mu_a$  images to obtain the final image. (4) Next, we search for suspicious clusters using full width half maximum (FWHM) of the updated  $\mu_a$  values within the prostate region. If no suspicious segment is identified, we conclude that the prostate has a low probability of having cancer.

In step 3, if some suspicious clusters in step 2 are seen, we then group all the non-suspicious clusters as one new single segment and subdivide the suspicious clusters into further smaller clusters. Now, the initial unit volume size used within the suspicious regions in step 3 is set to  $0.5 \times 0.5 \times 0.5 \text{ cm}^3$ . The procedure explained in step 2 is repeated here with a length variation of 0.25 cm in any one of three dimensions. Similar to step 2, the final reconstructed image of step 3 will be an average of the 8 images ( $j=8$ ) obtained by varying the unit volume in 8 different fashions. FWHM of the  $\mu_a$  values is still used to localize suspicious regions for further inspection with an improved spatial resolution.

Finally in step (4), the hard prior method was used to improve the optical properties of the suspicious regions identified in step 3. The initial guess here is the uniform initial guess as in step 1.

### Computer simulations

To validate HCM, we performed computer simulations by considering a mesh, which was anatomically similar to a TRUS prostate image, consisting of four different ROIs, such as prostate, peri-prostate tissue, rectum wall and prostate tumors. Two spherical shaped inclusions were placed with a horizontal separation of 20 mm and a vertical depth of 20 mm from the

surface of the rectal wall (Fig. 9). The rectum wall had a thickness of 5 mm and a curvature radius of 50 mm.

In step 1, as the prior location of prostate cancer is often not visible in TRUS images, we assumed homogeneous optical properties for all ROIs. A simulated TRUS-DOT probe was used, having 16 bifurcated optodes that could serve as both sources and detectors (Fig. 9a).

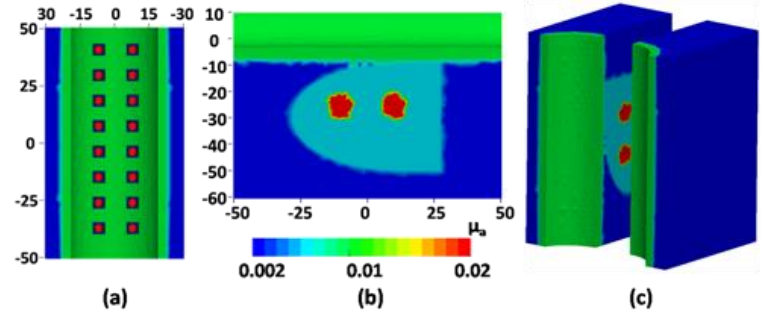


Figure 9: (a) Probe geometry used in the simulation; each optode is bifurcated to serve as a source and detector. (b) Two anomalies separated by 20 mm at a depth of 20 mm. (c) Mesh has been sliced in isometric view to show the simulation geometry.

The CW mode was utilized in the simulations; 1% random noise was added to the data to mimic the instrument noise. Simulated NIR data was computed along the rectum boundary using a FEM-based diffusion forward model with NIRFAST [11]. The first-step reconstruction was done using the initial guess of  $\mu_a=0.01 \text{ mm}^{-1}$  to recover the optical property of the prostate (Fig. 10a). Then, the reconstructed data from the first step served as the initial guess for the second and third steps. All reconstructions would stop when the change in projection errors is less than 2% of the previous iteration. Next, the prostate tissue was divided into several clusters. As noted earlier, the final image obtained after step 2 was the average over 16 independently reconstructed images, as demonstrated in Fig. 10b. In this simulation, we found an estimated suspicious region, as marked by the dotted rectangle in Fig. 10b, using FWHM. In step 3, the suspicious region identified in step 2 was further divided into smaller clusters. The final image of step 3 shown in Fig. 10c was the average over 8 reconstructed images. FWHM was used and resulted in two suspicious regions, which were treated as two individual regions and entered in the hard prior method for finer reconstruction in step 4.

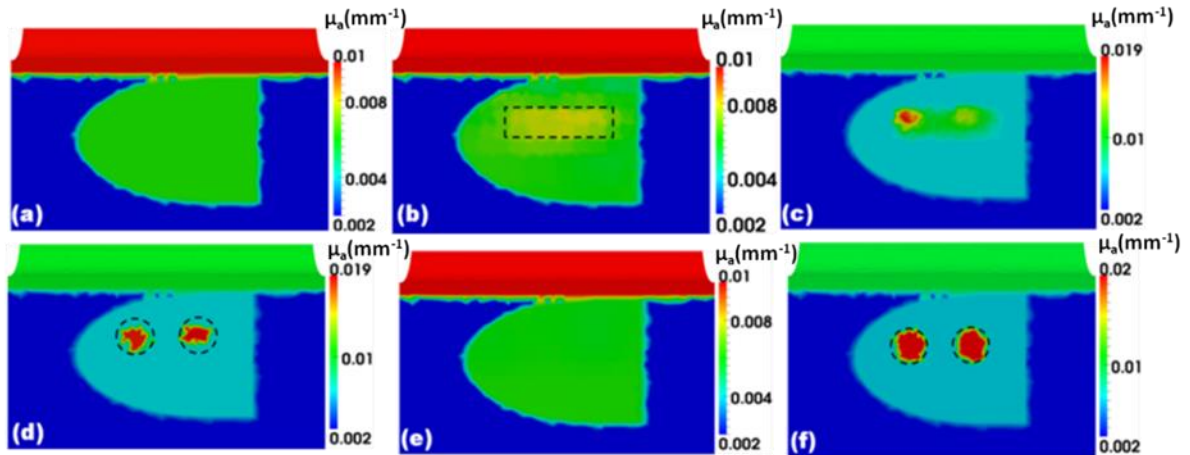


Figure 10: reconstructed  $\mu_a$  values in  $\text{mm}^{-1}$  using different reconstruction steps. The dotted circles indicate the real locations of the anomaly. Reconstructed image (a) after step 1 using HCM, (b) after step 2 using HCM; dotted rectangle indicates the suspicious location selected using FWHM, (c) after step 3 using HCM, (d) after step 4 using HCM. (e) Reconstructed image without any inclusions, but reconstructed using HCM. (f) Reconstructed image for the same case using a known hard prior for the inclusions.

### 2.2.3 Measurement system and data processing

### Instrumentation

For demonstrating HCM experimentally, we utilized the setup depicted in Fig. 11. A broadband pulsed laser source (SC-450, Fianium Inc., Eugene, Oregon) with a max output power of 40 mW (measured at the tip of an optical fiber) was utilized as the illumination source. Although the pulsed laser has a repetition rate of 20 MHz, due to the limited frequency response of the photodiodes, we still considered our system as a CW system. The laser output was collimated and fed through a filter wheel where a desired wavelength of 780nm was selected. In order to calibrate the fluctuations from the laser source, a beam sampler (BS) was utilized, and a sample beam was fed into another photodiode (PD) for further calibration. The light was again coupled into another optical fiber and fed into a multiplexor. The multiplexor, as controlled by a computer, illuminated 8 locations on an optode probe sequentially. We employed silica optical fibers (core diameter of 600  $\mu\text{m}$ ) for light delivery.

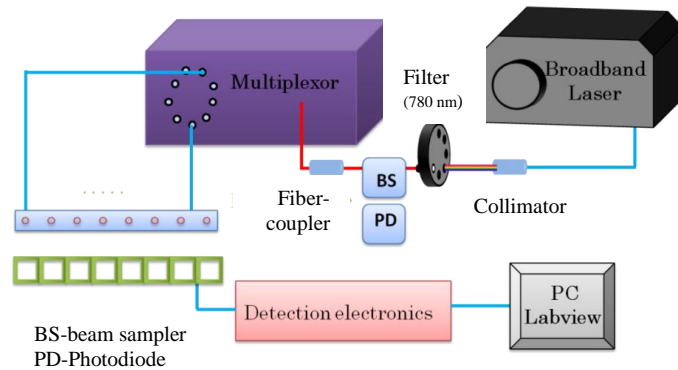


Figure 11: Instrumentation and probe setup utilized for laboratory phantom experiment.

For the detection electronics (Fig. 12), we utilized photodiodes (OPT101, Burr-Brown Corp., Tucson, Arizona) to collect the diffused light. An analog low pass filter (LPF) was employed to filter out unwanted higher frequencies. Next, the electrical signal was amplified using an operational amplifier in the inverting mode. The operational amplifier's gain was controlled by changing the resistance of feedback resistor. For digital control of gain, a digital potentiometer was utilized such that the gain was controlled from the computer. Next, the electrical signal was further fed into a buffer amplifier which itself was an operational amplifier in non-inverting mode with unity gain. Finally, we utilized a National Instruments DAQ card with 16-bit resolution to convert analog signals into digital format and stored in the computer. The proposed instrument setup, including scanning mechanism, electrical gain, and data acquisition, was controlled using Labview software.

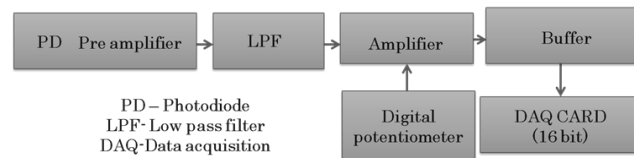


Figure 12: Flow chart depicting various stages of detection electronics utilized in proposed

### Experimental setup

Although in the computer simulations, we demonstrated our HCM using a multilayered model, we utilized a single layer phantom for experimental demonstration. We preferred a single layered phantom because of the complexity involved in the preparation of a multilayered phantom. Using a single layered phantom with an absorber inside, we skipped Step 1 in our reconstruction technique and directly started the reconstruction from step 2. The reason for skipping Step 1 was that it involved inducing the prior information; for this particular case, we did not use any prior information. The phantom setup is depicted in Fig. 13. A homogeneous liquid tissue-mimicking phantom was prepared by filling a container of dimensions of  $15 \times 10 \times 10 \text{ cm}^3$  with 1% Intralipid solution. This solution served as the homogeneous background medium with an absorption coefficient ( $\mu_a$ ) of  $0.1 \text{ cm}^{-1}$  and reduced scattering coefficient ( $\mu'_s$ ) of  $10 \text{ cm}^{-1}$ . A

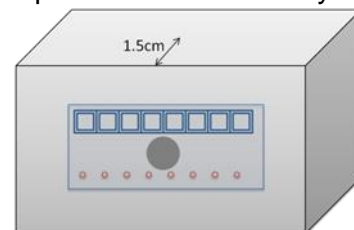


Figure 13: Experimental setup used in the laboratory phantom measurement.

spherical absorbers ( $\mu_a = 0.3 \text{ cm}^{-1}$ ) of 1-cm diameter were placed at 1.5-cm distance around the center of an optode array which was placed from one side surface of the container (Fig. 13).

### Experimental results

Panels in Fig. 14 provide overall comparisons among the reconstructed images that were obtained using the experimental setup given in Figs. 11-13. Figure 14(a) demonstrates the result obtained from the regular iterative DOT reconstruction technique. While this figure shows relatively good reconstruction in both location and size for the embedded absorber, we see very poor recovery in absorption contrast for the reconstructed object: the reconstructed value of  $\mu_a$  was  $0.012 \text{ cm}^{-1}$  while the expected value was  $0.03 \text{ cm}^{-1}$ . As seen in Fig. 14(b), step 2 in our HCM is able to determine the probable location of the absorber; Figs. 14(c) and 14(d) show the gradual improvement in the contrast recovery. By the end, both location and absorption contrast of the embedded absorber were reconstructed much better to meet the expected values.

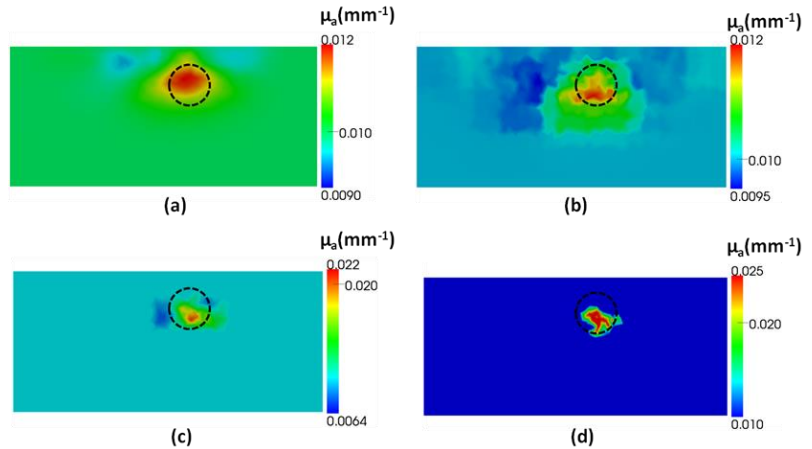


Figure 14: reconstructed  $\mu_a$  values and maps in  $\text{mm}^{-1}$  (a) using regular iterative DOT reconstruction technique and HCM after (b) step 2, (c) step 3, and (d) step 4.

### 2.3 Optical properties of human prostate specimens quantified by ex vivo measurements

Since our developed methodology depends highly on distinct differences in optical properties between benign/normal prostate tissues and prostate cancer tissues, we made some efforts to quantify and determine whether the cancer tissues do have significant differences in light absorption and scattering coefficients from those in normal prostate tissues. For this task, we shared existing resources and effort sponsored by an NIH grant to obtain insightful conclusions. Specifically, we conducted light reflectance spectroscopy (LRS) measurements between 500-840 nm from *ex vivo* fresh human prostate specimens right after prostatectomy on both normal and cancerous lesions, followed by data analysis using a quantitative model to determine hemoglobin concentrations and light scattering. For LRS, we took  $n=724$  distinct locations from both prostate capsular ( $n_c=185$ ) and parenchymal ( $n_p=539$ ) tissues, including prostate cancer (PCa) tissue, benign peripheral zone tissue and benign prostatic hyperplasia (BPH), of fresh *ex vivo* radical prostatectomy specimens from 37 patients with high volume, intermediate-to-high-grade PCa (Gleason score,  $GS \geq 7$ ). LRS parameters from parenchymal tissues were analyzed for statistical testing and classification. A feature selection algorithm based on multinomial logistic regression was implemented to identify critical parameters in order to classify high-grade PCa tissue. The regression model was in turn used to classify PCa tissue at the individual aggressive level of  $GS=7,8,9$ . Receiver operating characteristic curves were generated to determine classification accuracy for each tissue type. Please see Appendix B for details.

The conclusion for this part of study is that prostate cancer does have distinct and significant difference in light scattering from that of normal prostate tissue, which provides us with biomarkers and/or image contracts for ultrasound-coupled diffuse optical imaging.

### 3. Key Research Accomplishments and Reportable Outcomes

#### Key research accomplishments:

- (1) We have shown the feasibility of TRUS-DOT through computer simulations and laboratory phantom experiments.
- (2) We have designed a TRUS-compatible, DOT-based image system (780nm), in which the photo diodes were placed on the trans-rectal probe. Optical signals were recorded and used for estimating the absorption coefficient.
- (3) We validated the system using laboratory phantoms. For improved image reconstruction, we have also developed a hierarchical clustering method (HCM) to improve the accuracy of image reconstruction with limited prior information.
- (4) We have quantified and confirmed that prostate cancer does have distinct and significant difference in light scattering from that of normal prostate tissue, which provides us with biomarkers and/or image contracts for ultrasound-coupled diffuse optical imaging.

#### Reportable outcomes:

- (1) Peter LeBoulluec, Hanli Liu, and Baohong Yuan, "A cost-efficient frequency-domain photoacoustic imaging system," *Am. J. Phys.* Vol. 81, 712 (2013); doi: 10.1119/1.4816242
- (2) Venkaiah C. Kavuri and Hanli Liu, "Development of multispectral transrectal ultrasound compatible near infrared imaging system for early detection of prostate cancer," SPIE, Photonics West, BIOS Biomedical Optics Symposium, paper 8578-57, Feb. 2-7, 2013, San Francisco, California.
- (3) Vikrant Sharma, Ephrem O. Olweny, Payal Kapur, Jeffrey A. Cadeddu, Claus G. Roehrborn, and Hanli Liu, "Prostate cancer detection using combined auto-fluorescence and light reflectance spectroscopy: *ex vivo study of human prostates*," *Biomedical Optics Express*, Vol. 5(5), 1512-1529 (2014).

### 4. Conclusions

As mentioned by the end of Section 2.1, we have modified our original goals or ideas by developing transrectal ultrasound-guided diffuse optical tomography (TRUS-DOT) for improved prostate cancer imaging. In Sections 2.2, we have shown the feasibility of TRUS-DOT through computer simulations and laboratory phantom experiments. Specifically, we have designed a TRUS-compatible, DOT-based image system (780nm), in which the photo diodes were placed on the trans-rectal probe. Optical signals were recorded and used for estimating the absorption coefficient. We validated the system using laboratory phantoms. For improved image reconstruction, we have also developed a hierarchical clustering method (HCM) to improve the accuracy of image reconstruction with limited prior information. Then, in Section 2.3, we summarized our recent findings that prostate cancer does have distinct and significant difference in light scattering from that of normal prostate tissue, which provides us with biomarkers and/or image contracts for ultrasound-coupled diffuse optical imaging.

## 5. References

---

1. L. V. Wang, "Multiscale photoacoustic microscopy and computed tomography," *Nature Photonics* 3, 503-509 (2009).
2. M. Xu, and L. Wang, "Photoacoustic imaging in biomedicine," *Review of Scientific Instruments* 77, 041101 (2006).
3. K. Maslov and L. V. Wang, "Photoacoustic imaging of biological tissue with intensity-modulated continuous-wave laser," *Journal of Biomedical Optics* 13 (2008).
4. P. Leboulluec, B. Yuan, and H. Liu, "A compact and cost-efficient frequency-domain photoacoustic imaging technique," *American Journal of Physics*, 81, 712 (2013); doi: 10.1119/1.4816242.
5. J. Kandukuri, Y. Liu, and B. Yuan, "A cost-efficient and multi-functional system for ultrasound measurement and imaging," (2012).
6. L. Wang and H. Wu, *Biomedical Optics: Principles and Imaging*, John Wiley & Sons (2007).
7. S. Telenkov, A. Mandelis, B. Lashkari, and M. Forcht, "Frequency-domain photothermoacoustics: Alternative imaging modality of biological tissues," *Journal of Applied Physics* 105, 102029 (2009).
8. G. Xu, D. Piao, C. H. Musgrove, C. F. Bunting, and H. Dehghani, "Trans-rectal ultrasound-coupled near-infrared optical tomography of the prostate, part I: simulation," *Optics express* 16, 17484-17504 (2008).
9. P. K. Yalavarthy, B. W. Pogue, H. Dehghani, C. M. Carpenter, S. Jiang, and K. D. Paulsen, "Structural information within regularization matrices improves near infrared diffuse optical tomography," *Optics Express* 15, 8043-8058 (2007).
10. H. Dehghani, B. W. Pogue, J. Shudong, B. Brooksby, and K. D. Paulsen, "Three-dimensional optical tomography: resolution in small-object imaging," *Appl. Opt.* 42, 3117-3128 (2003).
11. H. Dehghani, M. E. Eames, P. K. Yalavarthy, S. C. Davis, S. Srinivasan, C. M. Carpenter, B. W. Pogue, and K. D. Paulsen, "Near infrared optical tomography using NIRFAST: Algorithm for numerical model and image reconstruction," *Communications in numerical methods in engineering* 25, 711-732 (2009).

# APPARATUS AND DEMONSTRATION NOTES

The downloaded PDF for any Note in this section contains all the Notes in this section.

Frank L. H. Wolfs, *Editor*

*Department of Physics and Astronomy, University of Rochester, Rochester, New York 14627*

This department welcomes brief communications reporting new demonstrations, laboratory equipment, techniques, or materials of interest to teachers of physics. Notes on new applications of older apparatus, measurements supplementing data supplied by manufacturers, information which, while not new, is not generally known, procurement information, and news about apparatus under development may be suitable for publication in this section. Neither the *American Journal of Physics* nor the Editors assume responsibility for the correctness of the information presented.

Manuscripts should be submitted using the web-based system that can be accessed via the *American Journal of Physics* home page, <http://ajp.dickinson.edu> and will be forwarded to the ADN editor for consideration.

---

## A cost-efficient frequency-domain photoacoustic imaging system

Peter LeBoulluec, Hanli Liu, and Baohong Yuan<sup>a)</sup>

*Department of Bioengineering, The University of Texas at Arlington, Arlington, Texas 76019 and Joint Biomedical Engineering Program, The University of Texas at Arlington and The University of Texas Southwestern Medical Center at Dallas, Texas 75390*

(Received 14 September 2010; accepted 8 July 2013)

Photoacoustic (PA) imaging techniques have recently attracted much attention and can be used for noninvasive imaging of biological tissues. Most PA imaging systems in research laboratories use the time domain method with expensive nanosecond pulsed lasers that are not affordable for most educational laboratories. Using an intensity modulated light source to excite PA signals is an alternative technique, known as the frequency domain method, with a much lower cost. In this paper, we describe a simple frequency domain PA system and demonstrate its imaging capability. The system provides opportunities not only to observe PA signals in tissue phantoms but also to acquire hands-on skills in PA signal detection. It also provides opportunities to explore the underlying mechanisms of the PA effect. © 2013 American Association of Physics Teachers. [<http://dx.doi.org/10.1119/1.4816242>]

### I. INTRODUCTION

Optical imaging of cancer has been intensively studied in recent years due to its unique and high sensitivity to endogenous and exogenous tumor contrast.<sup>1,2</sup> These optical techniques are usually limited either in penetration depth, e.g., a few hundred of microns for optical microscopy, or in spatial resolution, e.g., a few millimeters for optical diffuse optical tomography (DOT).<sup>1-3</sup> Obviously, a tradeoff exists between the imaging depth and spatial resolution.<sup>4</sup> To overcome this limitation, ultrasound techniques have been combined with optical approaches, yielding various diagnostic techniques such as photoacoustic (PA) imaging.<sup>4</sup> Using PA techniques, the ratio of imaging depth to spatial resolution can reach values up to about 100, which is  $\sim 10$  times higher than what can be achieved with conventional DOT. PA techniques can potentially be used for imaging cancers in human breast, prostate, skin, thyroid, neck, head, and others areas.<sup>4</sup> PA techniques provide optical contrast, which is usually much more sensitive to functional and molecular information of the tissue than ultrasound techniques, making it possible to measure the concentrations of total hemoglobin, oxy- and deoxy-hemoglobin, and specific molecules regulating tumor growth and metastasis.<sup>4,5</sup> Compared with pure optical imaging methods, such as DOT, PA techniques have much higher spatial resolution and similar imaging depth.<sup>4,5</sup> The basic

mechanism of the PA effect can be briefly explained as follows: (1) tissue absorbs the energy of light illumination; (2) the absorbed energy leads to a local temperature rise in the tissue; and (3) a pressure or sound wave, called the PA signal, is generated due to the thermoelastic effect.<sup>4</sup>

Most PA imaging systems in large research laboratories use a nanosecond pulsed laser with high pulse energy. A short light pulse avoids energy loss due to thermal energy diffusion before the generation of PA signals, which is known as thermal confinement.<sup>6</sup> A nanosecond pulsed laser with high pulse energy typically costs tens of thousands of dollars and is usually positioned on a large optical table. Low cost and compact PA imaging techniques that do not rely on nanosecond pulsed laser systems are useful for educational and research laboratories with limited resources and for global healthcare.<sup>7-11</sup> In this study, we have developed a frequency-domain PA (FD-PA) imaging system by using an inexpensive laser diode, a conventional single element ultrasound transducer, and a lock-in amplifier to improve the signal-to-noise ratio.<sup>12-16</sup> The theory and the experimental implementation of FD-PA have been extensively described in the literature.<sup>8,10,11,17</sup> A simple, compact, and cost efficient FD-PA imaging system is an excellent teaching and research tool for educators and researchers. It allows students and the general public to understand the underlying mechanisms of the PA effect and its applications, such as cancer imaging.

## II. FUNDAMENTAL THEORY OF FREQUENCY-DOMAIN PHOTOACOUSTICS

The wave equation used to quantify photoacoustic pressure is usually expressed as follows:

$$\left(\nabla^2 - \frac{1}{v^2} \frac{\partial^2}{\partial t^2}\right)P = \frac{-\beta}{C_P} \frac{\partial H}{\partial t}, \quad (1)$$

where  $P$  represents the photoacoustic signal,  $H$  is the laser heating function,  $v$  is the speed of sound,  $\beta$  is the thermal expansion coefficient, and  $C_P$  is the heat capacity per unit mass at constant pressure of the irradiated medium. In the

frequency domain, the laser intensity is usually modulated as a sinusoidal function with frequency  $f$ . Assuming the amplitude of the modulated intensity is  $I_0$ , the heating function can be expressed as:

$$H = \mu_a I_0 \exp(-i\omega t), \quad (2)$$

where  $\omega = 2\pi f$  and  $\mu_a$  is the absorption coefficient of the medium, which is usually proportional to the absorber concentration in the sample. When considering an infinitely long and optically thin planar or cylindrical absorber, the generated PA waves in the frequency-domain can be represented by

$$P = \frac{i\mu_a \beta I_0 v l}{2C_P} \left[ \frac{\text{sinc}(\hat{q})}{\sin(\hat{q}) + i\hat{\rho}\hat{v} \cos(\hat{q})} \right] \exp(-i\hat{q}\hat{t}), \quad (\text{planar absorber}) \quad (3)$$

$$P = \frac{i\mu_a \beta I_0 v a}{C_P} \left[ \frac{J_1(\hat{q})H_0^{(1)}(\hat{v}\hat{r}\hat{q})/\hat{q}}{J_1(\hat{q})H_0^{(1)}(\hat{v}\hat{q}) - \hat{\rho}\hat{v}J_0(\hat{q})H_1^{(1)}(\hat{v}\hat{q})} \right] \exp(-i\hat{q}\hat{t}), \quad (\text{cylindrical absorber}) \quad (4)$$

where  $l$  is the thickness of the slab,  $a$  is the radius of the cylinder, and  $\hat{r}$  is the radial coordinate.  $J_0$  and  $J_1$  are the zeroth and first-order Bessel functions, respectively.  $H_0^{(1)}$  and  $H_1^{(1)}$  represent the zeroth- and first-order Hankel functions, respectively.  $\hat{q}$  is the dimensionless frequency and  $\hat{t}$  is the dimensionless time. For a slab,  $\hat{q} = \omega l/2v$  and  $\hat{t} = 2v(t - \frac{z-1/2}{v})$ . For a cylinder,  $\hat{q} = \omega a/v$  and  $\hat{t} = vt/a$ .  $\hat{\rho} = \rho_{in}/\rho_{out}$  and  $\hat{v} = v_{in}/v_{out}$  are the dimensionless density and speed-of-sound parameters, respectively. The subscripts “in” refers to inside the absorber and “out” refers to outside the absorber. For a small spherical absorber with radius  $a$ , the PA wave can be expressed as

$$P = \frac{i\mu_a \beta I_0 v a}{C_P(r/a)} \left[ \frac{[\sin(\hat{q}) - \hat{q} \cos(\hat{q})]/\hat{q}^2}{(1 - \hat{\rho})(\sin(\hat{q})/\hat{q}) - \cos(\hat{q}) + i\hat{\rho}\hat{v} \sin(\hat{q})} \right] \times \exp(-i\hat{q}\hat{t}), \quad (5)$$

where  $\hat{q} = \omega a/v$  and  $\hat{t} = (\frac{v}{a})(t - \frac{r-a}{v})$ .

Using Eqs. (3)–(5), the following can be concluded about the strength of the FD-PA signal: (1) it is a sinusoidal function of time with the same frequency  $\omega$  as that of the modulated light; (2) it is proportional to the optical absorption coefficient  $\mu_a$  of the medium; (3) it is proportional to the amplitude of the modulated intensity  $I_0$ ; and (4) it depends on the modulation frequency  $\omega$  via  $\hat{q}$ .<sup>18,19</sup> In this study, the sample setup can be assumed to be a cylindrical absorber, described by Eq. (4).

## III. MEASUREMENT SYSTEM AND DATA PROCESSING

### A. Measurement system

Figure 1 shows the experimental setup. A function generator (FG, Agilent 33120A, Agilent Tech) generates a sinusoidal voltage signal of frequency  $f$  and a synchronized TTL (Transistor-Transistor Logic) signal with the same frequency

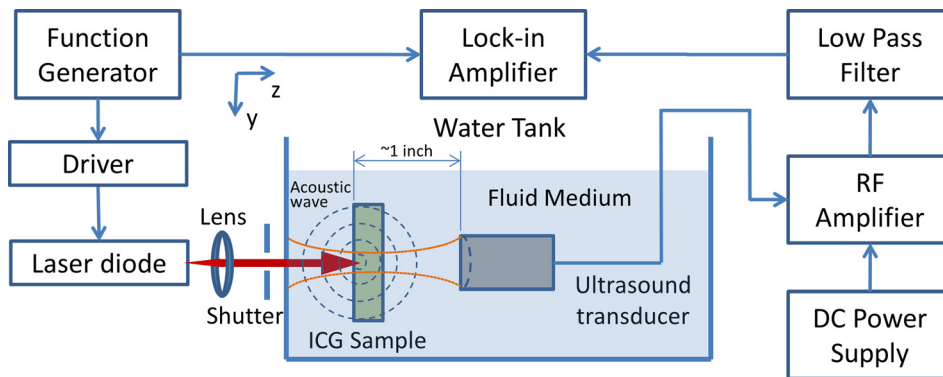


Fig. 1. The experimental setup used for PA imaging. The tank with the ICG sample is filled with either water or an intralipid solution. The function generator provides a sinusoidal voltage signal to the driver of the laser diode. A shutter is used to block the laser in order to measure the background noise. The modulated light is absorbed by the sample, causing the emission of PA waves, which are detected by the ultrasound transducer. The output voltage signal from the transducer is amplified, filtered, and sent to the lock-in amplifier.

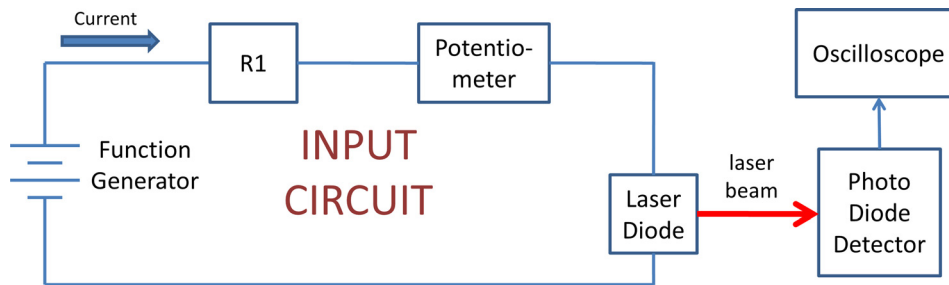


Fig. 2. Schematic of the modulation circuit used in our setup. The function generator provides DC and AC power to the circuit. The resistor and the potentiometer are chosen to provide a modulated current within the current range of the laser diode. The photodiode detector and oscilloscope are used to verify the modulation.

and a fixed phase shift. The sinusoidal signal is sent to a homemade circuit, shown in Fig. 2, to drive the laser diode (L785P100, Thorlabs). Thus, the laser intensity is modulated with the frequency  $f$ . The laser diode has a central wavelength of 785 nm and a power of  $\sim 100$  mW when operating in DC mode. A lens is used to collimate the laser beam and a mechanical shutter is used to manually block the laser illumination to measure the background signal. The synchronized TTL signal from the FG is sent to a lock-in amplifier (LIA, SR844, Stanford Research Systems) and used as a reference signal. The sample and ultrasound transducer (UST, Olympus NDT, 1 in. inch focal length) are submerged into a transparent 10-gal tank (20 cm wide, 40 cm long, and 24 cm high), filled with either water or an intralipid solution. The sample used is an indocyanine green (ICG) aqueous solution, which is injected into a partially optically and acoustically transparent tube (MRE-095, Braintree Scientific) that is vertically positioned in the tank. The outer and inner diameters of the tube are 2.5 and 1.7 mm, respectively. The UST is focused on the sample. Both the lateral and axial sizes of the focal zone, normally measured in terms of the full width at half maximum (FWHM), depend on the central frequency of the UST. When the intensity-modulated laser reaches the optically absorbing sample, a PA wave is generated. The PA wave is detected and converted into a voltage signal by the UST and further amplified (ZFL-1000LN, Mini Circuits) and filtered (SLP-5+, Mini Circuits). A total gain of 40 dB is applied by using two identical amplifiers in series, driven by a DC power supply (BK Precision 1506). The low pass filter (SLP-5+, Mini Circuits) is not required because the LIA has a very narrow bandwidth. The processed PA signal is delivered to the LIA and the amplitude of the PA signal and the phase difference between the PA signal and the reference signal are displayed on the screen of the LIA.

Figure 2 shows the principle of the modulation circuit. By generating an AC signal with a DC offset, the FG can serve as a DC and AC power source. A resistor (R1) and a potentiometer are used to limit and control the current flowing into the laser diode, respectively. The laser diode has a typical threshold current of 35 mA. The DC offset of the FG is  $V_{DC} = 2$  V and the AC peak-to-peak is  $V_{AC} = 4$  V. The total resistance of R1 and the potentiometer is about 11  $\Omega$ . A photodiode (EOT, ET-2030 A) is used to verify the modulation of the laser intensity via an oscilloscope (2530B Digital Storage Oscilloscope, BK Precision).

## B. Data processing

It is common that the LIA shows a background signal even when the laser is turned off or blocked. This background signal is mainly caused by electronic interference from the driving

signal generated by the FG. Fortunately, this background signal is independent of the location of the UST or the sample. A simple way to eliminate the effect of this background signal is to mathematically subtract it from the measured PA signal. Figure 3 schematically shows the relationship between the three signals, based on the amplitude and the phase measured with the LIA: (1) the measured signal, (2) the background signal, and (3) the PA signal. The angle between the vector representing each signal and the horizontal axis is the phase. The PA signal, vector (3) in Fig. 3, is the difference between the measured signal and the background signal. The magnitude of the PA signal is correlated with the optical absorption coefficient of the sample. All the calculations, image processing, and plotting were carried out using MATLAB (Mathworks), which is commonly used in engineering laboratories. Other software packages, such as MATHCAD, can be used as alternatives.

## IV. RESULTS AND DISCUSSIONS

Before the PA measurements, the laser beam was positioned to be coaxial with the UST. The tank was filled with a 1% intralipid solution to simulate biological tissues. The absorption and scattering coefficients of the intralipid solution are  $0.04 \text{ cm}^{-1}$  and  $8.4 \text{ cm}^{-1}$ , respectively, as measured with an ISS Oximeter. The tube was filled with an ICG aqueous solution, with a concentration of 0.5 g/l, to simulate an absorbing target. ICG is a relatively weak fluorophore in the near infrared range with a quantum yield of  $< \sim 1\%$  in aqueous media<sup>20</sup> and has been used as an optical absorber for PA imaging.<sup>21</sup> The laser diode and the UST were mounted on the same translation stage and their relative position was thus fixed. By moving the translation stage, the PA signal distributions along the x axis and in the x-y plane were acquired. Although the coaxial setup between the laser beam and the UST is not required, it improves the signal-to-noise ratio.

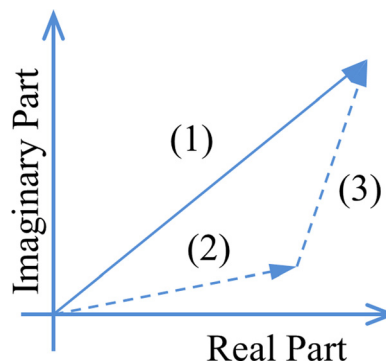


Fig. 3. The relation between the measured signal (vector 1), the background (vector 2), and PA (vector 3) signals.

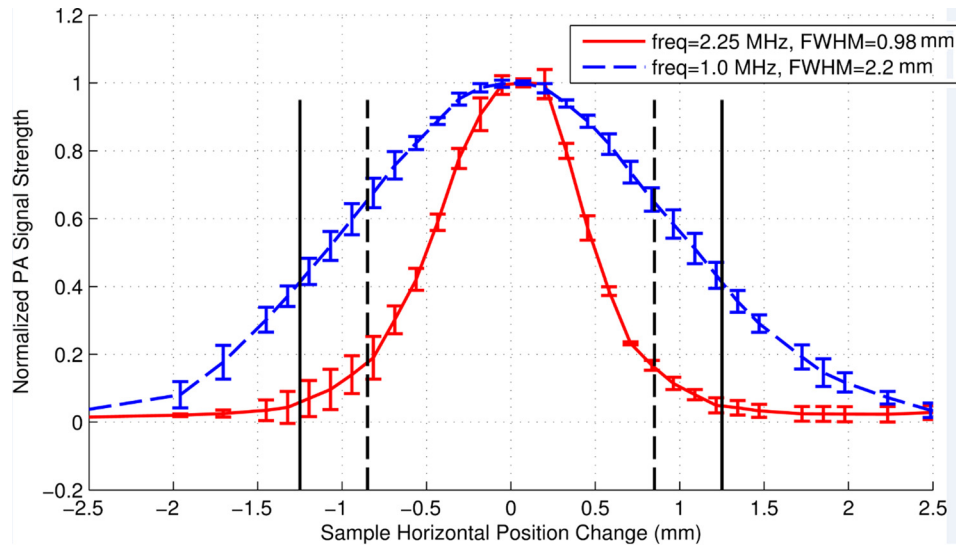


Fig. 4. The normalized PA signal strength as a function of the horizontal position of the sample relative to the co-axis of the laser beam and the UST. The data were obtained with a 1 MHz (dashed curve) and a 2.25 MHz (solid curve) UST. The dashed vertical lines show the inner diameters and the solid vertical lines show the outer diameters of the phantom tube that is filled with 0.5 g/l ICG solution at a depth of 1.9 mm in a 1% intralipid solution. The diameter of the collimated laser beam is  $\sim 1.0$  mm. The error bars represent the standard deviation of 4 measurements.

Figure 4 shows the strength of measured PA signal as a function of the horizontal position of the tube relative to the axis of the laser beam and the UST. The dashed and solid vertical lines represent the inner and outer diameter of the tube, respectively. Clearly, the strength of the PA signals rise when the laser beam gradually moves into the tube region and fall when the laser beam moves away from the tube region. These results indicate that the highly absorbing ICG tube generates significant PA signals compared to the surrounding intralipid solution that has a much lower absorption coefficient. The FWHM of the PA data using the 1 MHz UST, shown in Fig. 4, is about 2.2 mm. It is larger than the inner diameter of the tube (1.7 mm) and the UST lateral size (1.3 mm) since the FWHM is mainly determined by the convolution of the profiles of the cross section of the tube and the lateral focal zone of the UST.

When the frequency of the UST is increased from 1 to 2.25 MHz, the FWHM of the UST's lateral focal zone is reduced from  $\sim 1.3$  to  $\sim 0.72$  mm. The PA spatial resolution can be thus improved by using a higher frequency UST. Figure 4 shows that the FWHM of the PA signal measured with the 2.25 MHz UST is 0.98 mm which is smaller than the 2.2 mm width measured with the 1 MHz UST. However, the

width is smaller than the tube size and the reason is unclear. One possible reason may be that the PA signal generated from regions close to the edge of the tube is too weak to be detected. Higher frequencies provide smaller focal sizes and higher spatial resolution. A UST with a central frequency between 1 and 10 MHz achieves an acceptable spatial resolution. At frequencies below 1 MHz, the resolution will be degraded. Frequencies above 10 MHz will also work but increases the cost and the complexity of the system.

When the distance between the left-side of the tank wall and the left outer surface of the tube, defined as the depth of the tube, increases, the strength of the PA signal decreases. This is a consequence of the reduction in the light intensity reaching the sample due to the scattering in the medium. The dependence of the strength of the PA signal on the thickness or depth of the medium is shown in Fig. 5.

Increasing the ICG concentration increases the absorption coefficient of the tube, which raises the PA signal strength. Figure 6 shows the peak strength of the PA signal as a function of the ICG concentration. The PA signal strength increases when the concentration is increased but appears to saturate at high ICG concentrations. This may indicate that the light cannot penetrate into a highly concentrated ICG

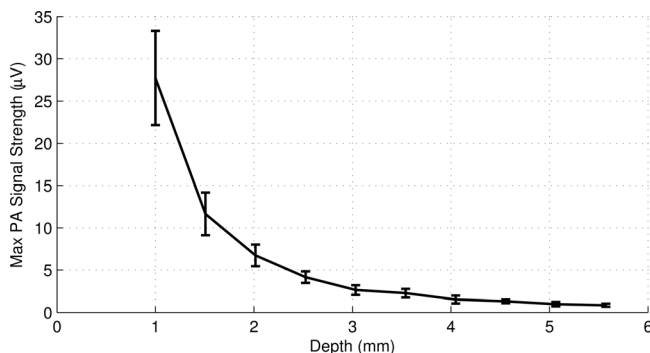


Fig. 5. The maximum PA signal strength as a function of the tube depth acquired with a 2.25 MHz UST in a 1% intralipid solution. The diameter of the laser beam is  $\sim 1.0$  mm and the ICG concentration is 0.5 g/l. The error bars represent the standard deviation of 4 measurements.

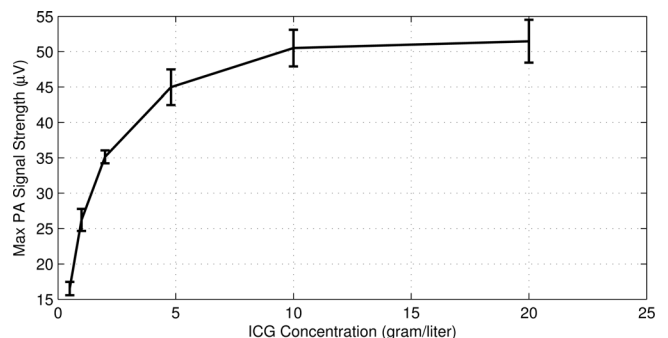


Fig. 6. The maximum PA signal strength as a function of the ICG concentration acquired with a 2.25 MHz UST in a 1% intralipid solution at a depth of 1.9 mm. The diameter of the collimated laser beam is  $\sim 1.0$  mm. The error bars represent the standard deviation of 5 measurements.

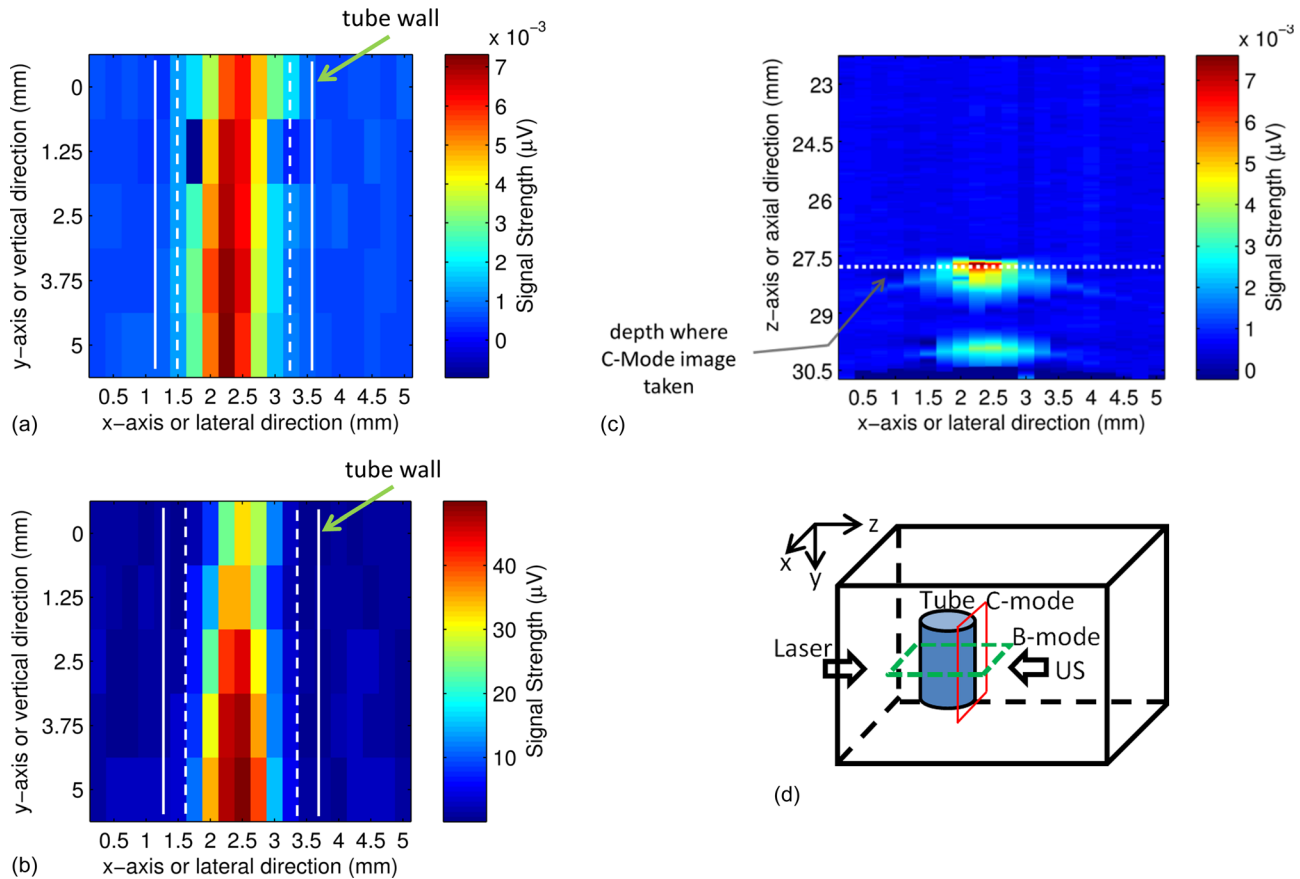


Fig. 7. (a) A C-mode ultrasound image and (b) a C-mode PA image of the ICG filled tube. The UST frequency is 2.25 MHz, the ICG concentration is 2 g/l, and the intralipid concentration is 1%. (c). An ultrasound B-mode image showing the cross section of the same ICG filled tube. The white dotted line indicates the depth of the C-mode images in (a) and (b). Note that the depth of zero in this figure is the surface of the UST, which is different from the definition of the tube depth). (d) A diagram to show the B-mode and C-mode imaging planes. The B-mode image is parallel to the x-z plane and the C-mode is parallel to the x-y plane (close to the right-side edge of the tube).

solution due to the large absorption coefficient, suggesting that the light absorption is confined to a limited region of the ICG solution.

Figures 7(a) and 7(b) show two-dimensional (2D) ultrasound and PA images of the tube in the x-y plane (C-mode, see Fig. 7(d) for the coordinates and the imaging plane). The ultrasound image was obtained with the same UST using the conventional pulse-echo method. The UST was connected to a pulse-generator-receiver (5073PR pulser/receiver, Olympus) and the reflected ultrasound data was acquired with the oscilloscope. The UST was raster scanned in the x-y plane. The laser was turned off because it is not used in ultrasound imaging. The reflected ultrasound echo signal at each location, also called the A-line, included the acoustic information along the z direction. After scanning the x-y plane, all A-lines can be used to construct a 3D image of the tube. Figure 7(a) shows a 2D image in the x-y plane, the so-called a C-mode ultrasound image, at a depth indicated by the white line in Fig. 7(c). Figure 7(c) shows a 2D image in the x-z plane, the so-called a B-mode ultrasound image, representing the cross section of the tube. The PA image shown in Fig. 7(b) was obtained with the system described in Fig. 1. This system does not have the capability to resolve the PA signal along z direction because the laser diode is continuously modulated. This is one disadvantage of the PA technique compared with the time-domain method. Therefore, only a 2D image in the x-y plane is shown in Fig. 7(b).

The data points shown in Figs. 7(a) and 7(b) were obtained by raster scanning the UST/laser system in the x-y plane. The step sizes in the lateral (x) direction and in the vertical (z) direction were 0.5 mm and 1.25 mm, respectively. Each rectangle represents the intensity of a single measurement. The two solid and dashed white vertical lines represent the outer and inner diameter of the tube, respectively. The average FWHM of the ultrasound image shown in Fig. 7(a) is about 0.98 mm, which is smaller than the inner diameter of the tube. Figure 7(b) shows the corresponding PA image in the x-y plane. The image clearly shows the tube with optical (absorption) contrast. The average FWHM is about 0.88 mm, which is also smaller than the inner diameter of the tube for reasons that are not clear.

Figure 7(c) shows the ultrasound image of the cross-section of the tube. To be consistent with conventional ultrasound imaging rules, zero depth in Fig. 7(c) is defined as the surface of the UST because that is the location where the ultrasound pulses are generated; note that this is different from the definition of the tube depth. The two bright areas show the two boundaries of the tube. Note that the inner boundaries of the tube cannot be resolved from this image due to the limited resolution of the UST (2.25 MHz). The dotted horizontal line in Fig. 7(c) indicates the depth of the ultrasound C-mode image shown in Fig. 7(a). Clearly, the ultrasound image shows the boundaries between the tube and the surrounding medium.

Table I. The major components of the PA system and their features, costs, and possible substitutes. The listed prices are for guidance only.

| Item                           | Model                   | Feature                                | Cost (USD)                  | Substitutes   |
|--------------------------------|-------------------------|--|-----------------------------|---|
| Lock-in amplifier              | SRS 844                 | Broadband 200 MHz                      | ~\$8,000                    | Regular LIA, <\$2000  |
| Function generator             | Agilent 33120 A         | Multiple function and 20 MHz bandwidth | ~\$1600                     | Regular FG, <\$1000   |
| Focused ultrasound transducer  | Olympus-NDT V314-SU-F   | Point focused, NA=0.375                | ~\$350                      | Other focused USTs with a central frequency between 1 and 10 MHz and reasonable sensitivity |
| Laser diode                    | Thorlabs L785P100       | 785 nm and 100 mw CW                   | ~\$40                       | Other laser diodes with power ~100 mw   |
| RF amplifiers (2x)             | Minicircuits ZFL-1000LN | Wideband, 0.1-1000 MHz                 | ~\$178<br>(2x at \$89 each) | Other RF amplifiers with a gain ~40 dB  |
| Low pass filter (not required) | Minicircuits SLP-5+     | Cutoff at 5 MHz                        | ~\$35                       | Other low pass filters with an appropriate cutoff frequency                                 |

## V. COST AND COMPACTNESS ANALYSES

Table I shows the general costs, features, and possible substitutes of the major components of the current PA system. The cost of the system is dominated by the cost of the LIA and the FG although lower cost LIAs and FGs could be adopted. Clearly, the cost of a FD-PA imaging system is much less expensive than that of a time-domain imaging system. The cost of the MATLAB software is not included in Table I. A student version of MATLAB is relatively cheap but other free or relatively inexpensive software packages can be used as alternatives. All components of the FD-PA system are compact. Although we have not attempted to reduce the overall size of our setup in the current study, it is possible to integrate the entire system into a small and portable box by replacing the FG and LIA with a small, customized circuit board. It will be extremely difficult for a time-domain PA system to achieve the same compactness.

## VI. CONCLUSIONS

A FD-PA imaging system was designed and its imaging capability was demonstrated with tissue-like phantoms. The imaging principle and data processing method were discussed. The measured PA signal strength depends on the absorption coefficient, the depth of the target, and the modulated light intensity of the laser diode. Appropriate processing of the measured PA data and background interference is an important key to correctly display the PA images. The lateral spatial resolution of PA images is dependent on the ultrasound frequencies and focal sizes of the ultrasound transducers. Although the current system has a low axial resolution due to the adopted ultrasound transducer, it can be significantly improved by using a high numerical aperture ultrasound transducer or by adopting a frequency-swept technique.<sup>9</sup> The FD-PA imaging system is cost effective compared to a time-domain imaging system.

## ACKNOWLEDGEMENTS

The authors acknowledge the funding support from DOD (W81XH-11-1-0231) and partially from NIH (7R15EB012312-02), CPRIT (RP120052), NSF (CBET-1253199) and seed grant of Research Enhancement Program from the University of Texas at Arlington.

<sup>a)</sup> Author to whom correspondence should be addressed. Electronic mail: baohong@uta.edu

<sup>1</sup>A. Corlu, R. Choe, T. Durduran, M. A. Rosen, M. Schweiger, S. R. Arridge, M. D. Schnall, and A. G. Yodh, "Three-dimensional in vivo fluorescence diffuse optical tomography of breast cancer in humans," *Opt. Express* **15**, 6696–6716 (2007).

<sup>2</sup>J. Culver, W. Akers, and S. Achilefu, "Multimodality molecular imaging with combined optical and SPECT/PET modalities," *J. Nucl. Med.* **49**, 169–172 (2008).

<sup>3</sup>D. M. McDonald and P. L. Choyke, "Imaging of angiogenesis: from microscope to clinic," *Nature Med.* **9**, 713–725 (2003).

<sup>4</sup>L. V. Wang, "Multiscale photoacoustic microscopy and computed tomography," *Nature Photon.* **3**, 503–509 (2009).

<sup>5</sup>L. H. V. Wang, "Ultrasound-mediated biophotonic imaging: A review of acousto-optical tomography and photo-acoustic tomography," *Dis. Markers* **19**, 123–138 (2004).

<sup>6</sup>M. Xu and L. Wang, "Photoacoustic imaging in biomedicine," *Rev. Sci. Instrum.* **77**, 041101 (2006).

<sup>7</sup>K. Maslov and L. V. Wang, "Photoacoustic imaging of biological tissue with intensity-modulated continuous-wave laser," *J. Biomed. Opt.* **13**, 024006 (2008).

<sup>8</sup>M. Euler, "Hands-on resonance-enhanced photoacoustic detection," *Phys. Teach.* **39**, 406–409 (2001).

<sup>9</sup>S. Telenkov, A. Mandelis, B. Lashkari, and M. Forcht, "Frequency-domain photothermoacoustics: Alternative imaging modality of biological tissues," *J. Appl. Phys.* **105**, 102029 (2009).

<sup>10</sup>W. F. Rush and J. E. Heubler, "Photoacoustic effect demonstration," *Am. J. Phys.* **50**, 669 (1982).

<sup>11</sup>M. Euler, K. Niemann, and A. Muller, "Hearing light," *Phys. Teach.* **38**, 356–358 (2000).

<sup>12</sup>P. A. Temple, "An introduction to phase sensitive amplifiers: An inexpensive student instrument," *Am. J. Phys.* **43**, 801–807 (1975).

<sup>13</sup>E. Wolfson, "The lock-in amplifier: A student experiment," *Am. J. Phys.* **59**, 569–572 (1991).

<sup>14</sup>J. H. Scofield, "Frequency-domain description of a lock-in amplifier," *Am. J. Phys.* **62**, 129–133 (1994).

<sup>15</sup>S. K. Sengupta, J. M. Farnham, and J. E. Whitten, "A simple low-cost lock-in amplifier for the laboratory," *J. Chem. Educ.* **82**, 1399–1401 (2005).

<sup>16</sup>K. Edmondson, S. Agoston, and R. Ranganathan, "Impurity level lifetime measurements using a lock-in amplifier," *Am. J. Phys.* **64**, 787–791 (1996).

<sup>17</sup>F. A. McDonald, "Photoacoustic effect and the physics of waves," *Am. J. Phys.* **48**, 41–47 (1980).

<sup>18</sup>M. I. Khan, T. Sun, and G. J. Diebold, "Photoacoustic waves generated by absorption of laser radiation in optically thin cylinders," *J. Acoust. Soc. Am.* **94**, 931–940 (1993).

<sup>19</sup>L. Wang, *Photoacoustic Imaging and Spectroscopy* (CRC Press, Boca Raton, 2009).

<sup>20</sup>T. J. Russin, E. I. Altinoglu, J. H. Adair, and P. C. Eklund, "Measuring the fluorescent quantum efficiency of indocyanine green encapsulated in nanocomposite particulates," *J. Phys. Condens. Matter* **22**, 334217 (2010).

<sup>21</sup>C. Kim, C. Favazza, and L. H. V. Wang, "In vivo photoacoustic tomography of chemicals: High-resolution functional and molecular optical imaging at new depths," *Chem. Rev.* **110**, 2756–2782 (2010).

# Prostate cancer detection using combined auto-fluorescence and light reflectance spectroscopy: *ex vivo* study of human prostates

Vikrant Sharma,<sup>1,2</sup> Ephrem O. Olweny,<sup>3</sup> Payal Kapur,<sup>4</sup> Jeffrey A. Cadeddu,<sup>3</sup> Claus G. Roehrborn,<sup>3</sup> and Hanli Liu<sup>1,2,\*</sup>

<sup>1</sup> Department of Bioengineering, University of Texas at Arlington, Arlington, TX 76019, USA

<sup>2</sup> Joint Program of Biomedical Engineering between University of Texas at Arlington and University of Texas Southwestern Medical Center at Dallas, Arlington, TX 76019, USA

<sup>3</sup> Department of Urology, University of Texas Southwestern Medical Center, Dallas, TX 75390, USA

<sup>4</sup> Department of Pathology, University of Texas Southwestern Medical Center, Dallas, TX 75390, USA  
\*hanli@uta.edu

**Abstract:** This study was conducted to evaluate the capability of detecting prostate cancer (PCa) using auto-fluorescence lifetime spectroscopy (AFLS) and light reflectance spectroscopy (LRS). AFLS used excitation at 447 nm with four emission wavelengths (532, 562, 632, and 684 nm), where their lifetimes and weights were analyzed using a double exponent model. LRS was measured between 500 and 840 nm and analyzed by a quantitative model to determine hemoglobin concentrations and light scattering. Both AFLS and LRS were taken on  $n = 724$  distinct locations from both prostate capsular ( $n_c = 185$ ) and parenchymal ( $n_p = 539$ ) tissues, including PCa tissue, benign peripheral zone tissue and benign prostatic hyperplasia (BPH), of fresh *ex vivo* radical prostatectomy specimens from 37 patients with high volume, intermediate-to-high-grade PCa (Gleason score,  $GS \geq 7$ ). AFLS and LRS parameters from parenchymal tissues were analyzed for statistical testing and classification. A feature selection algorithm based on multinomial logistic regression was implemented to identify critical parameters in order to classify high-grade PCa tissue. The regression model was in turn used to classify PCa tissue at the individual aggressive level of  $GS = 7, 8, 9$ . Receiver operating characteristic curves were generated and used to determine classification accuracy for each tissue type. We show that our dual-modal technique resulted in accuracies of 87.9%, 90.1%, and 85.1% for PCa classification at  $GS = 7, 8, 9$  within parenchymal tissues, and up to 91.1%, 91.9%, and 94.3% if capsular tissues were included for detection. Possible biochemical and physiological mechanisms causing signal differences in AFLS and LRS between PCa and benign tissues were also discussed.

©2014 Optical Society of America

**OCIS codes:** (170.1610) Clinical applications; (170.3650) Lifetime-based sensing; (170.6935) Tissue characterization; (170.4580) Optical diagnostics for medicine; (170.6510) Spectroscopy, tissue diagnostics.

## References and links

1. O. Yossepowitch, A. Bjartell, J. A. Eastham, M. Graefen, B. D. Guillonau, P. I. Karakiewicz, R. Montironi, and F. Montorsi, "Positive surgical margins in radical prostatectomy: outlining the problem and its long-term consequences," *Eur. Urol.* **55**(1), 87–99 (2009).
2. J. A. Wieder and M. S. Soloway, "Incidence, etiology, location, prevention and treatment of positive surgical margins after radical prostatectomy for prostate cancer," *J. Urol.* **160**(2), 299–315 (1998).
3. J. D. Sammon, Q. D. Trinh, S. Sukumar, P. Ravi, A. Friedman, M. Sun, J. Schmitges, C. Jeldres, W. Jeong, N. Mander, J. O. Peabody, P. I. Karakiewicz, and M. Harris, "Risk factors for biochemical recurrence following

- radical perineal prostatectomy in a large contemporary series: A detailed assessment of margin extent and location,” *Urol. Oncol.* **31**(8), 1470–1476 (2013).
4. A. Tewari and P. Narayan, “Novel staging tool for localized prostate cancer: a pilot study using genetic adaptive neural networks,” *J. Urol.* **160**(2), 430–436 (1998).
  5. L. W. D’Avolio, M. S. Litwin, S. O. Rogers, Jr., and A. A. Bui, “Automatic identification and classification of surgical margin status from pathology reports following prostate cancer surgery,” *AMIA Annu. Symp. Proc.* **2007**, 160–164 (2007).
  6. S. Salem, S. S. Chang, P. E. Clark, R. Davis, S. D. Herrell, Y. Kordan, M. L. Wills, S. B. Shappell, R. Baumgartner, S. Phillips, J. A. Smith, Jr., M. S. Cookson, and D. A. Barocas, “Comparative analysis of whole mount processing and systematic sampling of radical prostatectomy specimens: pathological outcomes and risk of biochemical recurrence,” *J. Urol.* **184**(4), 1334–1340 (2010).
  7. V. Iremashvili, S. D. Lokeshwar, M. S. Soloway, L. Pelaez, S. A. Umar, M. Manoharan, and M. Jordá, “Partial sampling of radical prostatectomy specimens: detection of positive margins and extraprostatic extension,” *Am. J. Surg. Pathol.* **37**(2), 219–225 (2013).
  8. H. Fukuhara, K. Inoue, H. Satake, K. Tamura, T. Karashima, I. Yamasaki, I. Tatsuo, A. Kurabayashi, M. Furihata, and T. Shuin, “Photodynamic diagnosis of positive margin during radical prostatectomy: preliminary experience with 5-aminolevulinic acid,” *Int. J. Urol.* **18**(8), 585–591 (2011).
  9. N. Lue, J. W. Kang, C. C. Yu, I. Barman, N. C. Dingari, M. S. Feld, R. R. Dasari, and M. Fitzmaurice, “Portable optical fiber probe-based spectroscopic scanner for rapid cancer diagnosis: a new tool for intraoperative margin assessment,” *PLoS ONE* **7**(1), e30887 (2012).
  10. B. Turkbey and P. L. Choyke, “Multiparametric MRI and prostate cancer diagnosis and risk stratification,” *Curr. Opin. Urol.* **22**(4), 310–315 (2012).
  11. V. Sharma, D. Kashyap, A. Mathker, S. Narvenkar, K. Bensalah, W. Kabbani, A. Tuncel, J. A. Cadeddu, and H. Liu, “Optical reflectance spectroscopy for detection of human prostate cancer,” *Conf. Proc. IEEE Eng. Med. Biol. Soc.* **2009**, 118–121 (2009).
  12. B. Kim, C. Temiyasathit, K. Bensalah, A. Tuncel, J. Cadeddu, W. Kabbani, V. Mathker, and H. Liu, “An efficient procedure for classification of prostate cancer in optical spectra,” *Expert Syst. Appl.* **37**, 3863–3869 (2010).
  13. G. Salomon, T. Hess, A. Erbersdobler, C. Eichelberg, S. Greschner, A. N. Sobchuk, A. K. Korolik, N. A. Nemkovich, J. Schreiber, M. Herms, M. Graefen, and H. Huland, “The feasibility of prostate cancer detection by triple spectroscopy,” *Eur. Urol.* **55**(2), 376–384 (2009).
  14. P. P. Dangle, K. K. Shah, B. Kaffenberger, and V. R. Patel, “The use of high resolution optical coherence tomography to evaluate robotic radical prostatectomy specimens,” *Int. Braz. J. Urol.* **35**(3), 344–353 (2009).
  15. L. Gao, H. Zhou, M. J. Thrall, F. Li, Y. Yang, Z. Wang, P. Luo, K. K. Wong, G. S. Palapattu, and S. T. Wong, “Label-free high-resolution imaging of prostate glands and cavernous nerves using coherent anti-Stokes Raman scattering microscopy,” *Biomed. Opt. Express* **2**(4), 915–926 (2011).
  16. Z. Jiang, D. Piao, G. Xu, J. W. Ritchey, G. R. Holyoak, K. E. Bartels, C. F. Bunting, G. Slobodov, and J. S. Krasinski, “Trans-rectal ultrasound-coupled near-infrared optical tomography of the prostate, part II: experimental demonstration,” *Opt. Express* **16**(22), 17505–17520 (2008).
  17. Z. Jiang, G. R. Holyoak, K. E. Bartels, J. W. Ritchey, G. Xu, C. F. Bunting, G. Slobodov, and D. Piao, “In vivo trans-rectal ultrasound-coupled optical tomography of a transmissible venereal tumor model in the canine pelvic canal,” *J. Biomed. Opt.* **14**(3), 030506 (2009).
  18. Z. Jiang, D. Piao, G. R. Holyoak, J. W. Ritchey, K. E. Bartels, G. Slobodov, C. F. Bunting, and J. S. Krasinski, “Trans-rectal ultrasound-coupled spectral optical tomography of total hemoglobin concentration enhances assessment of the laterality and progression of a transmissible venereal tumor in canine prostate,” *Urology* **77**(1), 237–242 (2011).
  19. V. C. Kavuri and H. Liu, “Hierarchical Clustering Method to Improve Transrectal Ultrasound-guided Diffuse Optical Tomography for Prostate Cancer Imaging,” *Acad. Radiol.* **21**(2), 250–262 (2014).
  20. R. J. Halter, A. R. Schmed, J. A. Heaney, and A. Hartov, “Passive bioelectrical properties for assessing high- and low-grade prostate adenocarcinoma,” *Prostate* **71**(16), 1759–1767 (2011).
  21. V. Backman, M. B. Wallace, L. T. Perelman, J. T. Arendt, R. Gurjar, M. G. Müller, Q. Zhang, G. Zonios, E. Kline, J. A. McGilligan, S. Shapshay, T. Valdez, K. Badizadegan, J. M. Crawford, M. Fitzmaurice, S. Kabani, H. S. Levin, M. Seiler, R. R. Dasari, I. Itzkan, J. Van Dam, and M. S. Feld, “Detection of preinvasive cancer cells,” *Nature* **406**(6791), 35–36 (2000).
  22. D. Elson, J. Requejo-Isidro, I. Munro, F. Reavell, J. Siegel, K. Suhling, P. Tadrous, R. Benninger, P. Lanigan, J. McGinty, C. Talbot, B. Treanor, S. Webb, A. Sandison, A. Wallace, D. Davis, J. Lever, M. Neil, D. Phillips, G. Stamp, and P. French, “Time-domain fluorescence lifetime imaging applied to biological tissue,” *Photochem. Photobiol. Sci.* **3**(8), 795–801 (2004).
  23. P. Crow, N. Stone, C. A. Kendall, R. A. Persad, and M. P. Wright, “Optical diagnostics in urology: current applications and future prospects,” *BJU Int.* **92**(4), 400–407 (2003).
  24. V. Sharma, S. Shivalingaiah, Y. Peng, D. Euhus, Z. Gryczynski, and H. Liu, “Auto-fluorescence lifetime and light reflectance spectroscopy for breast cancer diagnosis: potential tools for intraoperative margin detection,” *Biomed. Opt. Express* **3**(8), 1825–1840 (2012).

25. V. Sharma, J. W. He, S. Narvenkar, Y. B. Peng, and H. Liu, "Quantification of light reflectance spectroscopy and its application: determination of hemodynamics on the rat spinal cord and brain induced by electrical stimulation," *Neuroimage* **56**(3), 1316–1328 (2011).
  26. R. Richards-Kortum and E. Sevick-Muraca, "Quantitative optical spectroscopy for tissue diagnosis," *Annu. Rev. Phys. Chem.* **47**(1), 555–606 (1996).
  27. M. Y. Berezin and S. Achilefu, "Fluorescence lifetime measurements and biological imaging," *Chem. Rev.* **110**(5), 2641–2684 (2010).
  28. G. A. Wagnières, W. M. Star, and B. C. Wilson, "In vivo fluorescence spectroscopy and imaging for oncological applications," *Photochem. Photobiol.* **68**(5), 603–632 (1998).
  29. A. Bettelheim, H. Brown, K. Campbell, O. Farrell, and O. Torres, *Introduction to General, Organic and Biochemistry*, 10th ed. (Brooks/Cole, Cengage Learning, 2013).
  30. G. Zonios and A. Dimou, "Light scattering spectroscopy of human skin in vivo," *Opt. Express* **17**(3), 1256–1267 (2009).
  31. R. Nachabé, D. J. Evers, B. H. Hendriks, G. W. Lucassen, M. van der Voort, E. J. Rutgers, M. J. Peeters, J. A. Van der Hage, H. S. Oldenburg, J. Wesseling, and T. J. Ruers, "Diagnosis of breast cancer using diffuse optical spectroscopy from 500 to 1600 nm: comparison of classification methods," *J. Biomed. Opt.* **16**(8), 087010 (2011).
  32. M. M. Shen and C. Abate-Shen, "Molecular genetics of prostate cancer: new prospects for old challenges," *Genes Dev.* **24**(18), 1967–2000 (2010).
  33. D. A. Barron and D. R. Rowley, "The reactive stroma microenvironment and prostate cancer progression," *Endocr. Relat. Cancer* **19**(6), R187–R204 (2012).
  34. T. Hastie, R. Tibshirani, and J. H. Friedman, *The Elements of Statistical Learning: Data Mining, Inference, and Prediction*, 2nd ed. (New York, Springer, 2009).
  35. T. D. Wager, L. Y. Atlas, M. A. Lindquist, M. Roy, C.-W. Woo, and E. Kross, "An fMRI-Based Neurologic Signature of Physical Pain," *N. Engl. J. Med.* **368**(15), 1388–1397 (2013).
- 

## 1. Introduction

Improved capabilities for prostate cancer (PCa) detection during diagnosis and treatment would be highly beneficial to both urologists and patients, with potential applications in surgical margin assessment during radical prostatectomy and cancer monitoring during active surveillance. The former is particularly important considering that in a recent comprehensive review, positive surgical margins (PSM) during radical prostatectomy (RP) were noted to be present in up to 38% of cases [1]. While the clinical significance of PSM is variable, largely depending on margin extent and location, PSM is generally considered an adverse factor for disease-free survival [2,3]. Thus, minimizing PSM during RP will lead to a lower risk of biochemical recurrence and reduction of further therapeutic treatments. While much effort has been made in the field of pathological analysis [4–7] to improve the detection accuracy of PSM and extraprostatic extension, there have been very few technical reports [8] on development of optical techniques to detect PSM *in vivo* during RP or *ex vivo* right after retrieval of the excised prostate specimens. Very recently, Lue et al. have reported a portable optical fiber probe-based spectroscopic scanner for rapid cancer diagnosis [9]. While it is possible that such a scanner has the potential to become a clinical platform for intraoperative margin assessment, it is unknown whether optical signatures of PCa tissue are distinct enough to be differentiated from adjacent non-cancer tissues.

The second major issue in prostate cancer management is detection of early-stage biologically aggressive disease. Prostate specific antigen (PSA) screening has led to a significant rise in diagnosing the incidence of prostate cancer, which is currently diagnosed by transrectal ultrasound (TRUS)-guided prostate biopsy. Novel methods, such as multiparametric MRI, have demonstrated the potential for improved detection of high grade cancer and risk stratification in newly detected prostate cancers, but confirmatory biopsies are still required [10]. In addition, it is less likely or feasible to utilize MRI as a screening tool for detection of aggressive prostate cancer due to its complexity, availability, and cost, in comparison with a TRUS-guided, office-based, portable imaging device.

Several recent studies, including our own, have investigated the use of optical techniques for minimally invasive or non-invasive detection of PCa. As a simple, compact, and hand-held tool, optical reflectance spectroscopy was examined for optical signatures and feasible detection of PCa using *ex vivo* prostate specimens [11,12]. Salomon et al. [13] reported a

triple spectroscopy method in *ex vivo* prostate tissue with a sensitivity and specificity of 75% and 87.3%, respectively, for PCa detection. Dangle et al. explored the possibility of evaluating PCa tissue by high-resolution optical coherence tomography (OCT) [14], while Gao utilized a coherent anti-Stokes Raman scattering (CARS) microscope to image PCa tissue and cavernous nerves with cellular resolution [15]. From the non-invasive aspect, Jiang et al. demonstrated the feasibility to optically image PCa tissue and its surrounding vasculature using diffuse optical tomography (DOT) based on laboratory phantom measurements [16] and animal studies [17,18]. Recently, Kavuri and Liu reported the feasibility of imaging human PCa tissue by DOT without prior information on PCa locations using an optode geometry integrated with a transrectal ultrasound probe [19]. Furthermore, electrical impedance was also a possible bio-character to identify PCa. Halter et. al. [20] reported the use of electrical properties to differentiate PCa tissue from benign tissue, showing an area under curve (AUC) of 0.9 when discriminating between benign and malignant prostate tissue, 0.75 when discriminating between low and high grade cancer tissue.

In the present study, we developed and then evaluated a dual-modal optical device (*dMOD*), which incorporates dual measurements from auto-fluorescence lifetime spectroscopy (AFLS) and light reflectance spectroscopy (LRS) in a single fiber-optic probe of 1-mm diameter. LRS is sensitive to both tissue morphology and biochemical composition, while AFLS, on the other hand, captures the dynamic characteristics of endogenous fluorophores in the nanosecond range and is highly sensitive to the biochemical environment of the tissue. Each of these techniques has been successfully applied for identification of cancer tissue [21,22], but neither of them has been applied to human PCa diagnosis [23] nor studied as a combined technique for cancer detection. In principle, the vasculature, morphology and biochemical composition of PCa-bearing tissue are expected to differ from those of benign tissues; the differences are presumably more pronounced in higher grade and more advanced PCa tissue than slow-growing, less aggressive ones. Thus, we hypothesized in this study that LRS and AFLS, alone or in combination, could be able to detect and identify PCa at high grades.

Specifically, we performed dual-modal optical spectroscopic measurements from 37 *ex vivo* human prostate specimens right after radical prostatectomy. Measurements from twenty nine ( $n_p = 29$ ) out of the 37 glands were obtained from prostate parenchyma (i.e. tissue within the prostate capsules) and were used for characterization and classification of high grade PCa with Gleason score (GS)  $\geq 7$ . Measurements from the rest of the prostate specimens ( $n_c = 8$ ) were taken from capsular and extra capsular tissues. By the end of this study, we demonstrated that the *dMOD* is able to (1) discriminate high-grade PCa tissue (PCa) from benign peripheral zone prostate tissue (nPZ) and benign prostatic hyperplasia (BPH) in parenchymal tissues, and (2) result in excellent accuracy of above 90% in discriminating PCa from benign extra capsular tissues (ECT). In addition, several possible biochemical and physiological mechanisms were revealed and speculated to explain or interpret signal differences of AFLS/LRS induced by PCa. Overall, our results reported an excellent performance of this technique in its efficiency of detecting PCa at the individual Gleason grade from *ex vivo* human PCa-containing specimens.

## 2. Methods

### 2.1 Optical measurement setup and procedures

As reported earlier [24], the *dMOD* optical imaging system consisted of two modalities [Fig. 1(a)], namely AFLS and LRS, which were coupled through a custom-made fiber optic probe with 1-mm outer diameter (FiberTech Optica Inc., QC, Canada) [Fig. 1(b)], containing four fibers with different diameters [Fig. 1(c)]. The AFLS system consisted of a custom-made, single-channel, time correlated single photon counting system (ISS Inc., Champaign, IL)

machine and a pulsed supercontinuum laser source (5 ps, 20 MHz) (SC-450, Fianium Inc., Eugene, Oregon). This broadband laser light was filtered through a band pass filter at 447 nm with a bandwidth of 60 nm, as noted by 447 nm (60), and directed to the tissue sample for excitation. The auto-fluorescence signals and its corresponding lifetimes were measured using a photomultiplier tube (PMT) at four wavebands, namely, 532(10) nm, 562(40) nm, 632(24) nm, and 684(22) nm, each of which was selected sequentially through the emission filter wheel. Moreover, the LRS system consisted of a tungsten halogen light source (HL2000HP, Ocean Optics, FL), and a charged coupled device (CCD) array spectrometer (USB2000 + , Ocean Optics) that includes a spectral range of 500-840 nm, with a spectral sampling interval of 0.3 nm and a spectral resolution of 3 nm. More details on instrumentation is given in [24].

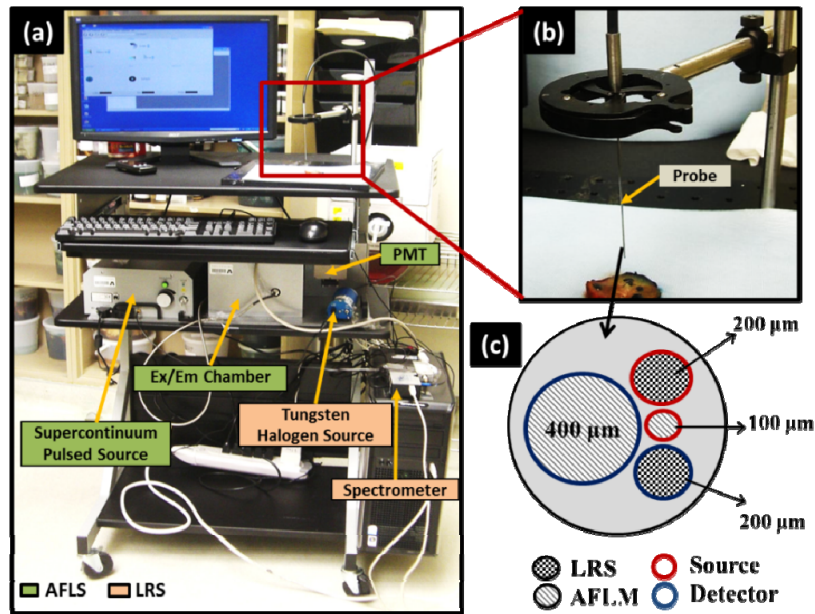


Fig. 1. Instrumentation: (a) Dual-modal optical system assembled on a portable cart for mobile capability to meet clinical needs; (b) close view of the optical probe positioned near the prostate specimen before actual optical readings; (c) front view of the probe showing arrangement of source and detector fibers for both AFLS and LRS.

## 2.2 Patients and surgical procedures

The study was conducted as per guidelines of the Institutional Review Board at the UT Southwestern Medical Center, Dallas, TX; each patient's informed consent was obtained before the surgery. Patients were selected with (a) an intermediate-to-high grade of disease ( $GS \geq 7$ ) and (b) a moderate-to-high volume of prostate cancer (at least two contiguous biopsy cores, each of which had 20% or more cancer involvement and/or bulky disease by endorectal MRI), so as to optimize spectral yield in this initial study. Each patient underwent robotic-assisted radical prostatectomy by one of two surgeons (JAC and CGR); then, the prostate glands were extracted after being disconnected from their blood supply for at least 30 minutes.

## 2.3 Experimental procedures

Resected prostate glands were immediately immersed in saline, and submitted for the dual-modal spectroscopy measurement [Fig. 2(a)]. For parenchymal tissue measurements, each of 29 glands ( $n_p = 29$ ) was first inked on the capsule first, as per standard protocol at UTSW for histological evaluation (blue for the left lobe; orange for the right lobe) [Fig. 2(b)]. Dyes were

fixed using acetic acid washes so that the ink on the capsule would not be transferred into the parenchymal tissues. Then, the specimens were cut in a coronal plane through the location of possible tumor nodules as determined by pre-surgery biopsy mapping, pre-surgery MRI and/or palpation, such that tumor nodules were highly likely to be visible at the cut cross sections [Fig. 2(c)]. When the cancer tissue was not clearly identified by visual inspection, a Diff quick-stained touch-prep slide was made of suspected cancer-bearing tissue, confirming the location of PCa cells cytologically. The locations of nPZ and BPH regions on the cut surfaces of the specimens were also identified.

The dual-modal optical system [Fig. 1(a)] was then introduced to start the measurements. The *dMOD* probe [Figs. 1(b) and 1(c)] was placed just in contact with the cut surface of the prostate gland, without pressing the gland, and LRS and AFLS spectra were recorded from each of the pre-specified regions (PCa, nPZ, and BPH) [Fig. 2(d)]. Given the wavelength range used, we expect that AFLM would sense the tissue depth within 1 mm. For LRS, the fiber diameter and the source-detector separation employed would give rise to a best sensitivity at 1-2 mm depth. Thus, both of them interrogated ~1 mm tissue in depth. Also, since our AFLM/LRS measurement was point-based, eight repeated measurements from adjacent spots were obtained in each region (3-5 mm in diameter) for each type of tissues (i.e., prostate cancer, normal, and BPH) from each specimen to account for tissue heterogeneity.

After all the optical measurements were complete, each measured region was then marked with black ink, and a thin (~1 mm thick) section of each measured region was separately removed and submitted for histological evaluation [Fig. 2(e)]. Hematoxylin and eosin stained sections from these sets of submitted tissue were evaluated by a urologic pathologist to confirm the presence and extent of PCa and to determine the corresponding Gleason grade. Measured spectra were further categorized into different grade groups according to the histologically confirmed results.

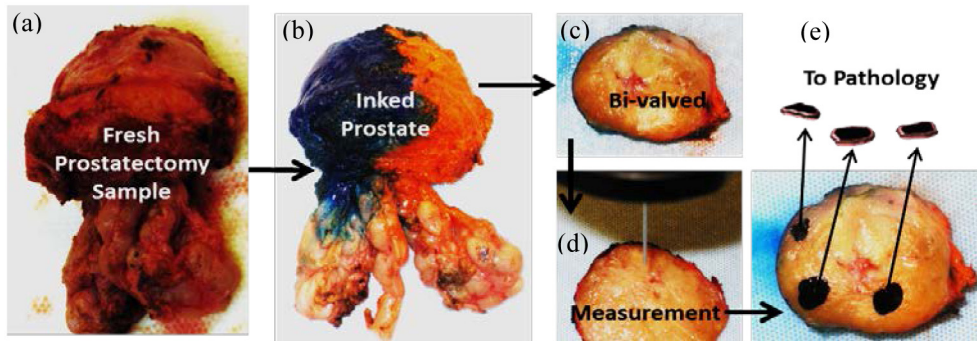


Fig. 2. Measurement Protocol: a freshly removed prostate specimen (a) was inked (b); then bi-valved in a coronal plane (c). After identifying benign peripheral zone tissue (nPZ), benign prostatic hyperplasia (BPH), and suspicious lesions for PCa, optical measurements were performed on the selected regions (d). Then, the measured regions were black-inked, removed, and sent for pathology confirmation (e), where black markings represent the removed tissue pieces that were optically measured and then sent for pathology analysis.

For capsular and/or extra-prostatic tissue measurements ( $n_c = 8$ ) on the gland capsules, freshly resected samples were randomly selected for measurement. The measurement protocol was the same as the one used for parenchymal tissue measurements, except that the prostate glands were measured before inking. Three types of extra capsular tissues (ECT) were measured, namely, tissues at the prostate base near the bladder, urethra at the prostate apex, and prostate capsular tissues. For each prostate gland, 2-3 regions of each type were identified, and five dual-modal optical readings were taken on each region. Given eight prostate specimens, each of which had 3-5 regions measured at five times, we had a total of

185 locations measured. Then, each of the measured regions was submitted to pathology for analysis; all capsular tissues were confirmed to be benign after histopathology examination.

#### 2.4 LRS and AFLS data processing for both PCa and benign tissues

A spectral width of 500-840 nm was chosen for data analysis; the corresponding data were fitted to a mathematical model [Eq. (1)], details of which have been described in [25].

$$R(\lambda) = \frac{\mu_s'(\lambda)}{k_1 + k_2\mu_a(\lambda)}. \quad (1)$$

Briefly,  $R(\lambda)$  is the measured spectral reflectance, which is associated with optical absorption and scattering coefficients ( $\mu_a$  and  $\mu_s'$ ) of the tissue by Eq. (1);  $k_1$  and  $k_2$  are instrument calibration constants. In principle, values of  $\mu_a$  result mainly from a variety of chromophores in tissue such as oxygenated hemoglobin (HbO), deoxygenated hemoglobin (Hb), total hemoglobin (HbT), and  $\beta$ -carotene within the measured tissues. Also, values of  $\mu_s'$  are closely related with cell size and density [25] and can be obtained at specific wavelengths. Thus, fitting Eq. (1) to the measured LRS data allowed us to obtain overall six LRS-based parameters including five fitted parameters (i.e., HbO, Hb, melanin,  $\beta$ -carotene, and light scattering coefficient at 750 nm) and one derived parameter ( $HbT = Hb + HbO$ ) per measured spot. For parenchymal tissue analysis, the absorption spectra of the surface inking dyes were also incorporated in the model to account for any contamination from the dyes during the slicing of the prostate tissue. Furthermore, when we utilized only LRS parameters for statistical testing and tissue classification, statistical differences in fitted parameters for PCa, nPZ and BPH were analyzed using a linear mixed model regression analysis implemented in SAS (SAS Institute Inc., Cary, NC, USA).

For AFLS, four auto-fluorescence decay curves corresponding to four emission wavelengths (see Section 2.1) were obtained at each measured spot/location. These curves were first normalized and then used to fit a two-exponent model, as described by Eqs. (2a) and (2b).

$$I(t) = a_1 \exp(-t/\tau_1) + a_2 \exp(-t/\tau_2) + c \quad (2a)$$

$$\tau_m = (a_1\tau_1^2 + a_2\tau_2^2) / (a_1\tau_1 + a_2\tau_2), \quad (2b)$$

where  $\tau_1$  and  $\tau_2$  represent the lifetime of two auto-fluorescence decay components,  $a_1$  and  $a_2$  are their respective weights, and  $c$  is a baseline offset. The integral-intensity-weighted mean lifetime ( $\tau_m$ ) was also calculated for each curve [24]. Thus, we obtained five fitted features for each of the four emission wavelengths, giving us overall 20 parameters per measured location. As in case of LRS, each of these features was analyzed for statistical differences between PCa vs. nPZ, and PCa vs. BPH, using a linear mixed model regression analysis.

#### 2.5 Classification and receiver operating characteristic (ROC) for parenchymal tissues

To examine the ability to discriminate PCa from benign tissue, two classification approaches were implemented. First, we tested the ability to differentiate prostate cancer (PCa, all grades combined) from benign nPZ and BPH using a 3-tissue-type classification model. Next, we evaluated the ability to differentiate individual grades of PCa with GS = 7, 8, 9 from benign nPZ and BPH using a 5-tissue-type classification model. These two classification approaches were evaluated for all three techniques, namely, LRS, AFLS, and *dMOD* (LRS + AFLS combined).

Specifically, we implemented a two-phase process for either 3-tissue-type or 5-tissue-type classification in order to effectively assess the classification accuracy for each technique. Phase one was to implement a feature selection algorithm so as to select a best feature set for cancer classification. In Section 2.4, we mentioned that fitting Eqs. (1), (2a) and (2b) to LRS

and AFLS data, respectively, would allow us to quantify multiple characteristic parameters or features (5 for LRS, 20 for AFLS, and thus 25 for *dMOD*), which could be utilized for PCa discrimination. However, all these features may not contribute equally and constructively to the classification model. An optimal feature set may allow better classification by reducing such problems as multicollinearity, redundancy, and overfitting of data. Thus, similar to our previous work [24], we employed sequential feature selection using a multinomial logistic regression model in this study. The actual determination of optimal features will be given in Section 3.1.

In phase two, for either 3-tissue-type or 5-tissue-type classification, we developed a multinomial logistic regression (MLR) model [24] along with 10-fold cross-validation [see Appendix] to classify respective types of prostate tissues and to obtain corresponding classification parameters for each tissue type. The procedures for this MLR-based classification are outlined in a flow-chart in Fig. 3, including (1) splitting data into 10 sub-groups; (2) using 90% of the data (*Tr*) for model training and 10% of the data (*Te*) for model testing; (3) generating an MLR-based classification model based on *Tr*; (4) generating ROC curves for each class of prostate tissues; (5) calculating the classification thresholds for PCa tissues; (6) testing the classification model derived from *Tr* with the independent data set, *Te*, by determining sensitivity (Sn), specificity (Sp), and accuracy (Acc); (7) performing ROC analysis based on MLR model and obtaining the area under curve (AUC) for each class of tissues; (8) repeating steps (2)-(7) 10 times using different sub-groups of *Tr* and *Te* for 10-fold cross validation and obtaining averaged Sn, Sp, Acc, and AUC; (9) repeating steps (1) - (8) 10 times after randomizing or regrouping the 10 sub-groups for *Tr* and *Te*, and thus achieving grand average values for means and standard deviation of Sn, Sp, Acc, and AUC. Note that the entire classification and ROC analysis were performed separately and independently for both 3-tissue-type and 5-tissue-type classification approaches.

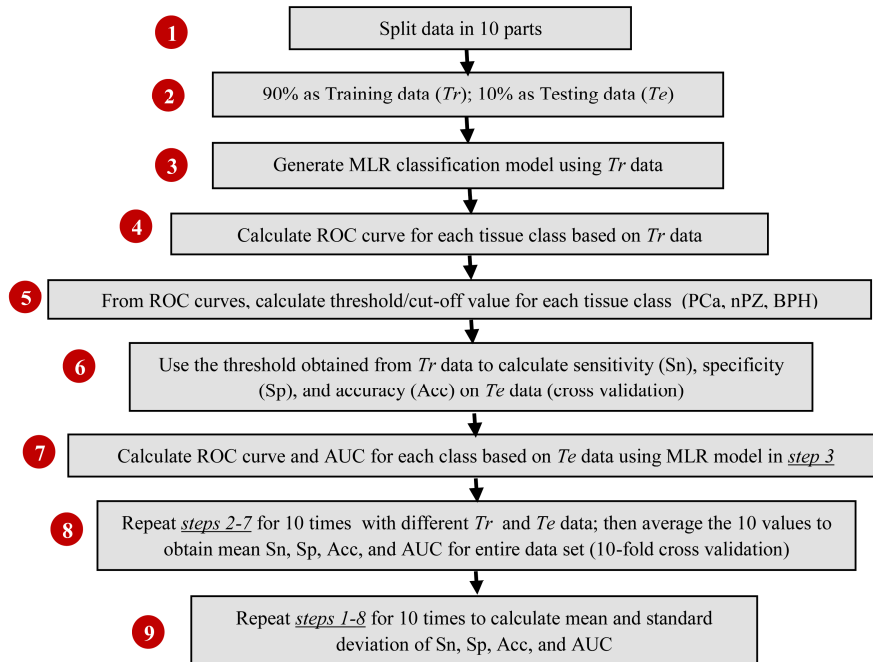


Fig. 3. A flow chart describing calculation of sensitivity, specificity, accuracy and generation of ROC curves through cross-validated classification process.

## 2.6 Data analysis for extracapsular tissues on the gland capsules

The data analysis procedures given in Sections 2.5 were used to analyze parenchymal tissues first; then they were repeated to investigate capsular and extra-capsular tissues. The same multinomial classification model with 10-fold cross validation was performed to evaluate the accuracy of *dMOD* to discriminate PCa from ECTs and nPZ. We again utilized 3-tissue-type and 5-tissue-type classification approaches to classify ECTs: the three tissue types included PCa, nPZ, and ECT; the five tissue types included PCa (GS 9), PCa (GS 8), PCa (GS 7), nPZ and ECT. Therefore, the 3-tissue-type classification method tested the accuracy in identifying any level of high grade PCa in presence of benign ECTs and nPZ tissue, whereas the 5-tissue-type classification tested the accuracy of differentiating specific high grade PCa at GS=7, 8, and 9 in the presence of benign ECTs and nPZ tissues.

## 3. Results

### 3.1 Results from prostate parenchymal tissues

A total of 29 patients were enrolled for this part of study (i.e., measurements from prostate parenchymal tissues); 6 out of 29 were excluded from the final analysis since their PCa tissues were made up only 25% or less over the entire tissue sampling evaluation, according to the final histology results. Mean (standard deviation) patient age was 60.7 (6.0) years. Several patients had multiple foci of PCa, resulting in 27 PCa regions, which were measured from 23 different prostate glands. As previously mentioned, 8 (or 9 from a few PCa regions) distinct spectral measurements were obtained from each region yielding a total of 221 PCa, 176 nPZ and 142 BPH measurements (see Table 1). Note that the numbers of measurements from nPZ and BPH reflect measurements from benign regions of the PCa-containing glands with the given GS.

Table 1. Number of measurements classified by tissue type\*

|                               | GS-7 | GS-8 | GS-9 | Total      |
|-------------------------------|------|------|------|------------|
| <b>N<sub>Subjects</sub></b>   | 13   | 4    | 6    | <b>23</b>  |
| <b>N<sub>Regions</sub></b>    | 15   | 5    | 7    | <b>27</b>  |
| <b>N<sub>meas</sub> (PCa)</b> | 125  | 40   | 56   | <b>221</b> |
| <b>N<sub>meas</sub> (nPZ)</b> | 104  | 32   | 40   | <b>176</b> |
| <b>N<sub>meas</sub> (BPH)</b> | 88   | 24   | 30   | <b>142</b> |

\* For each Gleason column, the number of measurements for PCa is approximately equal to  $N_{\text{Regions}} \times 8$ , with a few cases having nine repeated measures in the selected regions.

Analysis of means for AFLS data revealed that integral-intensity-weighted mean lifetimes ( $\tau_m$ ) for PCa were significantly ( $p < 0.05$ ) different from all other benign tissue types at all four wavelengths. While the lifetime of nPZ was shorter, BPH had a longer lifetime than PCa, consistently at all four wavelengths [Fig. 4(a)]. For LRS, analysis of means also showed statistical differences between PCa versus nPZ and PCa versus BPH for multiple fitted parameters [Fig. 4(b)]. Specifically, hemoglobin levels and  $\beta$ -carotene concentration were significantly smaller in PCa tissue than nPZ; BPH on the other hand showed significantly reduced deoxy-hemoglobin and  $\beta$ -carotene concentrations as compared to PCa tissue. One important observation is that light scattering was found significantly increased in PCa compared to all of the benign parenchymal tissues within prostate capsules.

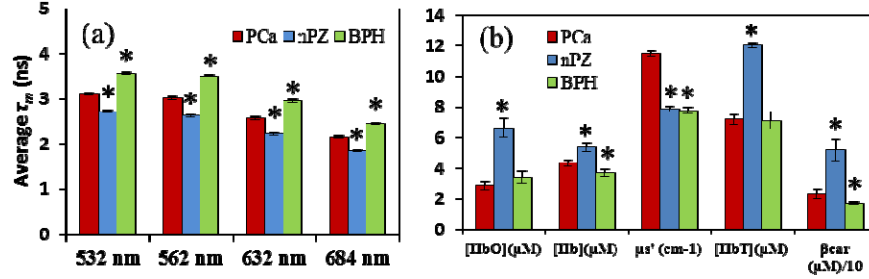


Fig. 4. (a) Comparison of four AFLS-derived mean-lifetimes,  $\tau_m$ , at all four emission wavelengths across three tissue types (PCa, nPZ, and BPH). (b) Comparison of five LRS-derived features across the three tissue types.  $\mu_s'$  was calculated at 750 nm, and  $\beta$ -car is scaled down by a factor of 10 for display purposes. For both (a) and (b), the symbol of '\*' above bars indicates a statistically significant difference ( $p < 0.05$ ) when compared to PCa. Error bars are based on standard error of mean.

In executing phase-one of data classification process (see Section 2.5) for AFLS only, the feature selection algorithm selected 15 out of 20 (i.e., 15/20) fitted AFLS parameters as an optimal feature set for 3-tissue-type classification, whereas 16/20 fitted AFLS parameters were selected for 5-tissue-type classification. For LRS only, all five parameters were selected by the feature selection algorithm for 'LRS only' classification and for both 3-tissue-type and 5-tissue-type classification. In case of dMOD, the selected feature number of parameters were 20/25 and 18/25 for 3-level and 5-level classification, respectively.

**Table 2. Classification metrics of PCa for parenchymal tissues, evaluated by LRS only, AFLS only, and dMOD (unit: %)**

| Classification method          | PCa Type                     | Mode | Sensitivity    | Specificity    | Accuracy                         | AUC*100                          |
|--------------------------------|------------------------------|------|----------------|----------------|----------------------------------|----------------------------------|
| 3-tissue-type classification*  | All high grade (GS $\geq$ 7) | AFLS | 64.2 $\pm$ 2.5 | 69.2 $\pm$ 1.8 | 67.1 $\pm$ 0.7                   | 72.9 $\pm$ 0.5                   |
|                                |                              | LRS  | 63.0 $\pm$ 1.5 | 82.9 $\pm$ 1.6 | 74.7 $\pm$ 1.0                   | 80.4 $\pm$ 0.2                   |
|                                |                              | dMOD | 79.0 $\pm$ 1.7 | 85.2 $\pm$ 1.1 | <b>82.7 <math>\pm</math> 0.7</b> | <b>90.8 <math>\pm</math> 0.4</b> |
| 5-tissue-type classification** | GS 9                         | LRS  | 84.4 $\pm$ 2.3 | 56.5 $\pm$ 0.7 | 59.4 $\pm$ 0.6                   | 72.9 $\pm$ 0.5                   |
|                                |                              | AFLS | 76.5 $\pm$ 3.2 | 75.9 $\pm$ 1.0 | 76.0 $\pm$ 0.9                   | 85.4 $\pm$ 0.6                   |
|                                |                              | dMOD | 82.3 $\pm$ 2.4 | 85.4 $\pm$ 0.7 | <b>85.1 <math>\pm</math> 0.6</b> | <b>91.5 <math>\pm</math> 0.7</b> |
|                                | GS 8                         | LRS  | 71.8 $\pm$ 2.6 | 72.6 $\pm$ 1.8 | 72.5 $\pm$ 1.6                   | 77.1 $\pm$ 0.7                   |
|                                |                              | AFLS | 76.3 $\pm$ 4.9 | 86.7 $\pm$ 0.8 | 86.0 $\pm$ 0.6                   | 90.0 $\pm$ 0.6                   |
|                                |                              | dMOD | 81.5 $\pm$ 3.4 | 90.8 $\pm$ 0.9 | <b>90.1 <math>\pm</math> 0.8</b> | <b>93.6 <math>\pm</math> 0.7</b> |
|                                | GS 7                         | LRS  | 71.9 $\pm$ 2.2 | 82.7 $\pm$ 1.3 | 80.2 $\pm$ 0.7                   | 87.9 $\pm$ 0.2                   |
|                                |                              | AFLS | 70.9 $\pm$ 2.0 | 72.4 $\pm$ 0.9 | 72.1 $\pm$ 0.7                   | 78.6 $\pm$ 0.7                   |
|                                |                              | dMOD | 86.0 $\pm$ 2.4 | 88.5 $\pm$ 0.7 | <b>87.9 <math>\pm</math> 0.6</b> | <b>94.7 <math>\pm</math> 0.4</b> |

\* The values listed in this category implicate the classification for all high-grade PCa tissue group against non-cancer tissue types (nPZ and BPH). \*\* The values listed in this category implicate the classification for each PCa tissue group (e.g., GS 9) against remaining tissue groups. All are high grade (GS $\geq$ 7).

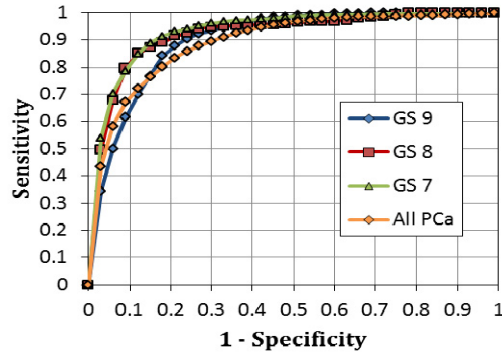


Fig. 5. ROC curves obtained using the *dMOD* and the MLR classification for identifying parenchymal PCa tissues at individual PCa grades (GS 9, GS 8, GS 7) using 5-tissue-type classification and with all grades combined (All PCa) using 3-tissue-type classification.

After generating the MLR classification models using selected features and completing phase-two data process for 3-tissue-type classification, we were able to evaluate classification accuracy by quantifying Sn, Sp, Acc, and AUC for all high-grade PCa (i.e., all  $GS \geq 7$  combined) with classification based on AFLS and LRS, individually or combined, as listed in Table 2. It is clear that *dMOD* gives rise to the best sensitivity (79.0%), specificity (85.2%), accuracy (82.7%), and AUC (90.8%) for PCa classification compared to either of the two techniques (AFLS and LRS). Furthermore, we repeated phase-two data process for 5-tissue-type classification, and the analysis outcome was also excellent as shown in Table 2. The authors' two-phase classification method allows identification of PCa tissue at the individual Gleason grade, namely,  $GS = 7, 8,$  and  $9,$  and to return the best classification performance by its sensitivity, specificity, accuracy and AUC for all three PCa grades. It is clear that *dMOD* is the optimal approach to be able to accurately classify not only PCa tissue but also its specific Gleason grade. Three corresponding ROC curves obtained by *dMOD* for respective Gleason scores are illustrated in Fig. 5. One extra ROC curve for all PCa grades combined, as determined by 3-tissue-type classification from *dMOD*, is also plotted in Fig. 5 for comparison. This figure reveals that the overall performance from 5-tissue-type classification is superior, particularly for PCa tissue with Gleason grades of  $GS=7$  and  $GS=8$  compared to 3-tissue-type classification.

### 3.2 Results from extra-capsular tissues on the gland capsules

For extra prostatic or extra capsular tissues (ECT), the measured AFLS/LRS data sets were taken from 185 small sites on or adjacent to the prostate capsules of additional eight patients. Analysis of means for AFLS data revealed that ECT lifetimes were closer to those of BPH and significantly longer than those from PCa. Also, in LRS, oxy- and total hemoglobin concentrations were significantly lower, whereas deoxy-hemoglobin concentration was significantly higher in PCa tissues than in benign ECT. In particular, light scattering of PCa at 750 nm was still significantly larger than that in benign ECT, which is very consistent with the case of parenchymal benign tissues (see Fig. 4).

**Table 3. Classification metrics to discriminate PCa from benign tissues (including ECT), evaluated by LRS only, AFLS only, and *dMOD* (unit: %)**

| Classification method          | PCa Type              | Mode        | Sensitivity | Specificity | Accuracy          | AUC*100 |
|--------------------------------|-----------------------|-------------|-------------|-------------|-------------------|---------|
| 3-tissue-type classification*  | All high grade (GS>7) | <i>AFLS</i> | 86.6 ± 1.7  | 79.4 ± 1.2  | 82.1 ± 0.8        | 92 ± 0  |
|                                |                       | <i>LRS</i>  | 76.7 ± 0.5  | 92.6 ± 0.7  | 86.6 ± 0.4        | 93 ± 0  |
|                                |                       | <i>dMOD</i> | 92.1 ± 1.0  | 92.4 ± 0.8  | <b>92.3 ± 0.5</b> | 98 ± 0  |
| 5-tissue-type classification** | GS 9                  | <i>LRS</i>  | 80.2 ± 2.0  | 78.2 ± 0.5  | 78.4 ± 0.3        | 85 ± 1  |
|                                |                       | <i>AFLS</i> | 88.1 ± 2.7  | 91.7 ± 0.2  | 91.4 ± 0.4        | 95 ± 1  |
|                                |                       | <i>dMOD</i> | 82.8 ± 1.8  | 95.5 ± 0.5  | <b>94.3 ± 0.5</b> | 96 ± 1  |
|                                | GS 8                  | <i>LRS</i>  | 70.3 ± 5.3  | 79.7 ± 0.8  | 79.1 ± 0.8        | 81 ± 0  |
|                                |                       | <i>AFLS</i> | 76.8 ± 2.1  | 92.3 ± 0.3  | 91.3 ± 0.3        | 93 ± 1  |
|                                |                       | <i>dMOD</i> | 83.5 ± 3.2  | 92.5 ± 0.3  | <b>91.9 ± 0.3</b> | 95 ± 1  |
|                                | GS 7                  | <i>LRS</i>  | 87.1 ± 2.3  | 80.4 ± 1.0  | 81.8 ± 0.8        | 92 ± 0  |
|                                |                       | <i>AFLS</i> | 83.3 ± 1.2  | 76.0 ± 0.9  | 77.5 ± 0.7        | 88 ± 0  |
|                                |                       | <i>dMOD</i> | 91.4 ± 1.4  | 91.0 ± 0.3  | <b>91.1 ± 0.3</b> | 97 ± 0  |

We utilized the same multinomial classification with 10-fold cross validation to evaluate the accuracy of *dMOD* to discriminate PCa tissues from ECTs and nPZ. The feature sets for 3-tissue-type classification included 11 features out of 20 from AFLS, all 5 features from LRS, and 23 parameters from the dual-modal method. Also, the feature sets for 5-tissue-type classification included 16, 5, and 16 fitted parameters from AFLS, LRS, and *dMOD*, respectively, after executing the feature selection algorithm. The final outcome of phase two classification analysis for both 3-tissue-type and 5-tissue-type classification is listed in Table 3. The former classification gave rise to 92.3% accuracy when identifying any level of high grade PCa (GS>7) in the presence of benign ECTs and nPZ tissue; the latter classification resulted in a range of accuracy between 91.1% to 94.3% when identifying high grade PCa by Gleason scores in the presence of these benign tissues. In comparison, *dMOD* offered overall excellent performance and better classification accuracy than each modality alone (i.e., either LRS or AFLS), as clearly demonstrated in the Table.

It is also noted that when being stratified by Gleason grade, AFLS data provided high accuracy of ~91% for both GS 9 and GS 8, which is comparable to the accuracy obtained by *dMOD*. However, the accuracy for identifying PCa with GS 7 is much better by *dMOD* (91%) than by either AFLS (77.5%) or LRS (81.8%). The analysis results given in Table 3 confirm that *dMOD* can provide excellent accuracy in discriminating high grade PCa (with or without identifying Gleason scores) from benign parenchymal and extra capsular tissues. The corresponding ROC curves determined by both 3-tissue-type and 5-tissue-type classification methods with *dMOD* data are shown in Fig. 6. Being consistent with Table 3, this figure reveals that the overall performances of these two classification methods are comparable, giving rise to high accuracy, as long as *dMOD* is utilized for data analysis and classification. Both Table 3 and Fig. 6 support that *dMOD* has great potential to be developed as an excellent tool for positive margin assessment during or right after radical prostatectomy, thus improving the management and treatment outcomes of PCa.

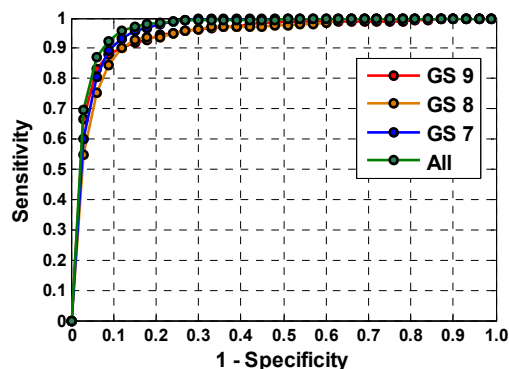


Fig. 6. ROC curves obtained using the *dMOD* and MLR classification for identifying PCa and ECTs at individual Gleason grades (GS 9, GS 8, GS 7) using 5-tissue-type classification and with all grades combined (All PCa) using 3-tissue-type classification.

#### 4. Discussion and conclusions

Optical imaging and measurement techniques are increasingly being developed, evaluated, and/or utilized for a broad range of medical applications. Of particular interest is their potential to differentiate benign from malignant tissue with high sensitivity and specificity. In particular, successful application of optical imaging techniques may have the potential to significantly impact current treatment paradigms for prostate cancer among others, improving diagnostic yield of prostate biopsies, monitoring of PCa foci within the prostate during active surveillance, and assessing surgical margins during radical prostatectomy. For these specific reasons, we hypothesized in the present study that a dual-modality optical method using AFLS and LRS has the ability to detect and differentiate high grade PCa tissues from benign, low-risk ones. To prove this hypothesis, we integrated a *dMOD* system, measured *ex vivo* human prostate glands, implemented feature selection and classification algorithms, and investigated the capabilities of discriminating high grade PCa from benign prostate tissues based on fitted parameters from AFLS and LRS, individually and in combination. In this section, we will discuss data classification algorithms, compare *dMOD* system performance, and compare our approaches with published methods. We will also discuss biochemical and/or physiological mechanisms resulting in signal differences of AFLS/LRS induced by PCa. Finally, we will discuss limitations of our proposed classification method.

##### 4.1 MLR classification models

Although several parameters in both LRS and AFLS exhibit significant differences between PCa and benign tissues, none of these parameters can be singly used to discriminate PCa from benign tissues. While these parameters are associated with anatomical or physiological or biochemical behaviors of the tissues, standard deviations of these parameters are quite high, which can be attributed to the heterogeneity of the tissues and insufficient intrinsic contrasts as well. The MLR algorithm was thus employed: first to identify critical features (using sequential feature selection [24]), followed by combining the selected features to create a decision model for identifying different tissue types (see Section 2.5).

Two different models were realized in this study: (1) 3-tissue-type classification for discriminating high grade PCa ( $GS \geq 7$ ) from benign tissues, and (2) 5-tissue-type classification for discriminating PCa stratified by Gleason scores. While the ability to identify high grade PCa is important, the ability to detect PCa at  $GS = 7$  is particularly more significant and clinically meaningful. This is because  $GS = 7$  is the critical landmark of aggressive PCa and marks the action timeline from active surveillance to aggressive treatment in order to have early treatment with effective outcomes. Therefore, our 5-tissue-type

classification method for identifying PCa stratified by Gleason scores is potentially more useful for future clinical applications.

#### 4.2 Performance of *dMOD* approach and comparison to published works

We hypothesized in the beginning of this study that LRS and AFLS, separately or in combination, could enable detection and identification of PCa tissue at high grades from either parenchymal tissues within prostate capsules or extra-prostatic tissues on or adjacent to the capsules. Our results proved that the *dMOD* approach, which combined LRS and AFLM for tissue classification analysis, gave rise to the highest accuracy for PCa tissue discrimination, in comparison to either technique alone for both intra-capsular as well as extra-capsular tissues.

When 3-tissue-type classification was performed on intra-prostatic tissues, our two-phase classification algorithm and ROC analysis showed that AFLS and LRS individually had discriminative accuracy of 67.1% and 74.7%, respectively. AFLS and LRS also had a similar sensitivity, but LRS had a higher specificity for detection of PCa without identifying cancer grade. When parameters from the two modalities were combined (*dMOD*), discriminative accuracy, sensitivity and specificity for PCa (all grades combined) were significantly improved (Table 2). Consistently, *dMOD* improved accuracy over those by the individual modalities for discriminating individual grades of PCa (GS = 7,8,9) with respect to the benign tissue (Table 2), when 5-tissue-type classification approach was performed. Similar conclusions were clearly held on extra-capsular data (Table 3), except that the classification accuracies from each of the two techniques were much higher than those in the intra-prostatic case. In fact, for GS of 8 and 9, AFLS results were almost comparable (though not as high) to *dMOD*, but Gleason 7 was significantly less accurate for AFLS alone.

Overall, it is clear from Tables 2 and 3 that classifying PCa stratified by Gleason scores considerably improved the classification accuracy in comparison with the all-grade-combined approach. This observation implies that PCa at different Gleason scores (i.e., at different aggressive levels) exhibits unique fluorescence and reflectance properties, which are closely associated with their respective biochemical and/or physiological mechanisms, which will be discussed in the next sub-section. This also makes the 5-tissue-type classification model be the method of choice for accurately identifying PCa.

While prior published reports on methods designed towards discriminating PCa tissues *in vivo* are limited, several optical studies using *ex vivo* prostate specimens have been found [13–15,20]. The study by Salomon et. al. [13] used a triple spectroscopy approach on frozen-thawed *ex vivo* prostate tissue (16 malignant and 75 benign samples) to discriminate malignant from benign tissue. Their technique involved spectral measurement and assessment from laser-induced auto-fluorescence, white-light remission, and high-frequency impedance spectroscopy. They reported a cross-validated sensitivity and specificity of 75% and 87.3%, respectively, which are comparable to our results. Halter et al. [20] measured electrical properties of 71 malignant and 465 benign *ex vivo* samples and reported a maximal accuracy of 81.8% for PCa tissues with  $GS \geq 7$ . In comparison, with *dMOD*, we obtained an accuracy of 82.7% for differentiation of PCa with  $GS \geq 7$  (Table 2) in parenchymal tissues, showing equal or better accuracies of PCa detection compared to the two methods aforementioned. Furthermore, two other optical technologies with high or cellular spatial resolution, OCT [14] and CARS [15], were explored recently as a potential imaging tool to identify positive PCa margins and/or cavernous nerves for guiding radical prostatectomy. While OCT provided a high image resolution in depth up to 1 mm, it seemed to lack physiology-based specificity, resulting in a fairly good sensitivity (70%) and specificity (84), excellent negative predictive value (96%), but a poor positive predictive value (33%) [14]. Since CARS is a microscope-based facility, it is able to image PCa and cavernous nerves at a cellular resolution. The results shown in [15] confirmed that CARS has the potential to become a clinical tool for surgical-margins assessment for PCa, while no classification of PCa at any GS was reported.

### 4.3 Origin and significance of measured parameters

#### 4.3.1 Fluorescence signals

It is well known that optical fluorescence is closely associated with biochemical components/compounds or metabolic status within tissues, so it has been utilized in the field of biomedical research for decades, with either intensity or lifetime measurements. Numerous reviews on this topic can be found in literature, and two examples are given in [26,27]. As we mentioned in our previous study [24], measurement of fluorescence lifetime provides much information on the mechanisms that lead to chemical or biochemical processes. Furthermore, each pair of excitation/emission (ex/em) light either matches or corresponds to a set of electron energy levels for a specific molecular structure or biochemical bond. It has been a common practice over the past few decades to select 350 nm/450 nm as the ex/em pair since this pair is directly linked to the oxidized form of nicotinamide adenine dinucleotide, which is a major electron acceptor. In its reduced form, it is called NADH. The reduced nicotinamide ring is fluorescent, which enables investigators to gain insight into the redox state of tissue and cellular metabolism [26]. Many studies have shown that the fluorescence signals from NADH are often reduced in tumor tissues due to a decrease in relative amount of NADH in malignant tissues [26].

In this study, however, we did not utilize NADH as an endogenous tissue fluorophore to probe PCa. We selected  $\lambda_{\text{ex}} = 447$  nm for several reasons: (1) to push the spectral window towards longer wavelengths than ultraviolet light in order to have a deeper light penetration depth, (2) to explore other biochemical components or processes that may be linked to PCa, and (3) to find other possible biomarkers (besides NADH) for high grade PCa detection. Throughout the study, our findings show that all fluorescence signals at  $\lambda_{\text{em}} = 532, 562, 632,$  and  $684$  nm have exhibited shorter lifetimes [see Fig. 4(a)] by PCa at all high grade levels ( $\text{GS} \geq 7$ ) than by the benign peripheral zone (nPZ) tissues. The next question is: What biochemical molecules are probed at these four wavelengths, and how are they affected by or associated with PCa?

Based on existing literature on *in vivo* fluorescence spectroscopy [28] and fluorescence lifetime, we expect that our selected excitation at 447 nm targets such endogenous fluorophores as lipopigments, flavins, and porphyrins within the prostate tissues. According to [28], porphyrin emission becomes dominant only after 600 nm, flavins have an emission peak between 500 and 600 nm, and lipopigments have a strong and broad emission band around ~450-700 nm (centered at ~560 nm). This implies that our detected fluorescence signals result from a combination of more than one fluorophore: specifically, both flavins and lipopigments contribute the fluorescence signals at 532 nm and 562 nm, while both lipopigments and porphyrins influence the signals at 632 nm. Indeed, the lifetimes observed at the respective four wavelengths in this study match well with those of key biochemical compounds [27] within lipopigments, flavins, and porphyrins. The key point in the following is to discuss and understand why high grade PCa alternate fluorescence signals and lifetimes of lipopigments, flavins, and porphyrins.

First, one major chromophore within lipopigments is lipofuscin, which consists of yellow-brown-colored granules and is marked as one of the aging or “wear-and-tear” pigments. Lipofuscin can be considered as a later phase of the cellular digestion chain associated with lysosomes, which are cellular, enzyme-containing organelles and serve as the stomach of the cell to process waste materials and cellular fragments [29]. Many diseases, such as macular degeneration, Alzheimer's disease, and Parkinson's disease, have been reported to have abnormal accumulations of lipofuscin. Thus, we speculate that high grade PCa tissue is likely to have ill-behaving lysosomes, which are not able to perform well cellular disposal function and thus lead to unhealthy accumulation of lipofuscin within the prostate tissue. Next, it is well known that flavin adenine dinucleotide (FAD) is a redox cofactor, playing a key role in cellular metabolism. FAD often exists in two different redox states: the oxidized form, FAD,

and reduced form, FADH<sub>2</sub> [29]. The former is fluorescent, while the latter one is not. It is often seen that the fluorescence signals from FAD are largely reduced in tumor tissue because of the decrease in the oxidized form of flavins. Last, since porphyrins are a group of organic compounds, one of which is heme, the pigment in red blood cells and a cofactor of the protein hemoglobin, we expect to see alternations in porphyrins fluorescence signatures due to diseased vasculature of PCa tissues. Given all the biochemical relations between the measured fluorescence signals and PCa, we conclude that our AFLS signals enable us to probe PCa status due to damaged or defective functions in cellular disposal and metabolic processes as well as ruined blood vasculature. Table 4 summarizes the relations between the measured fluorescence signals and biochemical compounds that are altered in their functions by PCa. This table implies that it might be possible to identify specific changes in lifetime from each of the three biochemical compounds/fluorophores, so as to reveal cellular or metabolic alternations due to PCa, by decomposition of lifetime decay signals. However, it is beyond the scope of this paper and will be explored in our future studies.

**Table 4. Summary of relations among fluorophores, cellular or metabolic functions, and expected versus measured fluorescence signals and lifetimes at emission wavelengths**

| Biochemical fluorophores in prostate tissue | Relations to cellular/metabolic functions of tissue | Fluorescence expected (spectral band; peaks) in nm [28] | Fluorescence measured [see Fig. 4(a)] ( $\tau$ : lifetime in ns) |                 |                 |
|---|---|---|--|-----------------|-----------------|
|   |   |   | Peak   | $\tau$ ; cancer | $\tau$ ; benign |
| Porphyrins                                  | Tissue vasculature                                  | > 600; 630, 680   | 632 nm   | 2.59 ±          | 2.22 ±          |
|   |   |   | 684 nm   | 0.49            | 0.45            |
|   |   |   |  | 2.17 ±          | 1.85 ±          |
| Flavins                                     | cellular metabolism                                 | 500-600; 550  | 532 nm   | 3.12 ±          | 2.72 ±          |
|   |   |   | 562 nm   | 0.44            | 0.37            |
|   |   |   |  | 3.03 ±          | 2.63 ±          |
|   |   |   |  | 0.48            | 0.38            |
| Lipopigments                                | cellular disposal process                           | 450-670; 560  | 532 nm   | 3.12 ±          | 2.72 ±          |
|   |   |   | 562 nm   | 0.44            | 0.37            |
|   |   |   | 632 nm   | 3.03 ±          | 2.63 ±          |
|   |   |   |  | 0.48            | 0.38            |
|   |   |   |  | 2.59 ±          | 2.22 ±          |
|   |   |   | 0.49   | 0.45            |                 |

While NADH is an endogenous tissue fluorophore to probe metabolic states of tissue and/or cancer, we investigated three other biochemical and molecular signatures of prostate cancer using AFLM with excitation at 447 nm and emission at 532, 562, 632, and 684 nm. Given the results in our previous study on breast cancer [24], we expect that the AFLM methodology demonstrated here is highly likely to work for cancer detection and classification in other types of cancer. Note that since the excitation-emission spectral bands of lipopigments, flavins, and porphyrins are rather broad, appropriate wavelengths for both excitation and emission can be possibly chosen in efficient spectral ranges depending on available optical hardware and choices of researchers.

#### 4.3.2 Reflectance signals

Origin of LRS signals has been well understood and described in the biomedical optics literature. Basically, both chromophore concentrations, such as HbO and Hb, and light scattering, which reflects cell sizes and densities, can be estimated quantitatively from direct LRS measurements [25]. Several reported studies have utilized LRS with small fiber geometry to investigate various tissue types and cancer [30,31]. The physiological significance of LRS-derived HbO, Hb, and other chromophores is self-evident as they provide absolute values of respective chromophore concentrations. Also, quantification of light scattering is directly associated with cell size and density: the larger and denser the particles

(such as cellular nuclei and intra-cellular organelles) are, the larger the light scattering coefficients are.

Our results in Fig. 4(b) clearly show that HbO, Hb, and HbT are all more prevalent in tissues within the benign peripheral zone, indicating overall better or fuller blood perfusions in the benign parenchymal tissues than in the PCa regions. Lower HbT values for PCa are also consistent with our previous work, taken from a different data set [11]. Furthermore, Fig. 4(b) also demonstrates that oxygen saturation ( $SO_2 = [HbO]/[HbT]*100$ ) was lowest in PCa (39.7%), as compared to nPZ (55.3%) and BPH (47.9%), indicating relative hypoxia in the PCa region, also consistent with our previous study [11].  $\beta$ -carotene was also found to be a contrast parameter for intra-prostatic tissues.

Moreover, as evident from Fig. 4(b), the light scattering coefficient (at 750 nm) of PCa was much higher than that of all benign tissue types consistently, resulting from morphological alternation in cellular size and density of PCa tissue. Indeed, it is suggested that as the PCa grade of tissue increases from low to high, glandular epithelial cells will progress toward prostatic intraepithelial neoplasia (PIN) and then become adenocarcinoma [32] with increased hyperplastic epithelium or/and cellular tufts filling the glandular space [33]. In the meantime, it was recently hypothesized that progression of PIN triggers reactive stroma formation, which is likely cancer-promoting, coevolves with foci of adjacent carcinoma, and thus changes cellular architecture and composition in both glandular and stroma space [33]. All of these morphological changes are the physiological origin to cause increases in light scattering.

#### 4.4 Limitations and future work

Despite the promising results shown above, a few limitations of our study warrant discussion. First, both AFLS and LRS readings were recorded from *ex vivo* tissues approximately one hour after the prostates were disconnected from any blood supply. Re-evaluation of our methodology under *in vivo* setting may yield different spectral outputs, particularly for the spectral signatures of HbO, Hb, and HbT, given *in vivo* hemodynamic perfusion conditions and complex biochemical microenvironments.

Second, our prostate specimen sample size was relatively small and limited to patients with high grade PCa at  $GS \geq 7$ . Since identification of PCa at  $GS = 7$  is highly critical in order to decide whether any treatment is needed, it is of necessity that the developed methodology needs to have high sensitivity and specificity. As such, further parameterization to characterize lower grades of PCa (i.e.,  $GS \leq 6$ ) should be mandatory prior to future clinical applications.

Third, the number of features used for *dMOD* tissue classification seems to be large and thus may lead to an overfitting concern. Because of non-perfusion conditions in our *ex vivo* prostate specimens, currently collected readings of HbO, Hb, and HbT may have large deviations due to a variety of physiological insults or defects. We expect that further *in vivo* studies may provide us with improved physiological conditions for the prostate glands during data collections, which in turn will reduce the deviations of fitted parameters and thus lead to a smaller number of features needed for accurate PCa classification.

Finally, our spectral signatures of PCa were all obtained within the prostate capsules (i.e., parenchyma tissues). Prior to *in vivo* applications, AFLS and LRS characteristic spectra of positive margins on prostate capsules will need to be identified and included for updated classification analysis.

Overall, this study was to investigate whether there exists any optical signature to discriminate PCa from non-cancerous prostate tissue and what kinds of optical signatures of PCa at different stages have. Much further development is needed before extending this technique to *in vivo* human environment. But, this study demonstrates that the *dMOD* methodology can be developed for *ex vivo* detection of positive margins in the operating room

during or right after radical prostatectomy, thus improving the management and treatment outcomes of PCa.

#### 4.5 Conclusions

This study has demonstrated that the *dMOD* approach, which combines auto-fluorescence and light reflectance spectroscopy, is able to discriminate PCa at Gleason grade 7 or higher from benign parenchymal tissue as well as from capsular or extra-prostatic tissue types of *ex vivo* prostate specimens with excellent classification sensitivity, specificity and accuracy. With further development and validation, the *dMOD* approach has the potential to be developed as an intraoperative aid for positive margin assessment during radical prostatectomy, a minimally invasive aid for active surveillance strategies, and a complementary/integrated tool for other clinical applications.

#### Appendix: Cross-validation [34]

**Cross-validation** is commonly used to validate a new classification model by assessing how accurate the classification results are when the model is tested with an independent data set [34]. In general, a classification model is developed using a given dataset of known data as the training dataset to serve as “ground truth”. Then, another independent dataset of unknown data is utilized as the testing dataset in order to test the model. In reality, the number of actual datasets is sometimes limited, so the testing results are not statistically conclusive. To solve this problem, k-fold cross validation is often employed by randomly partitioning the original datasets into k equal size subsamples. Next, a single subsample is kept as a testing dataset, while the remaining k – 1 subsamples serve as training data. To be statistically meaningful, this cross-validation process is performed k times, with each of the k subsamples rotated once as the validation or testing data. In a special case, where the measurement sample size, n, is relatively small, leave-one-out cross-validation is commonly used. Then, the independent, testing dataset is just one measurement; cross-validation will become an n-fold operation where n is the number of measurements. Specifically, we used 10-fold cross-validation in this study [see Fig. 3], with multiple data points in each training and testing datasets. Another example is given in ref [35], where leave-one-participant-out cross-validation was used to test their predication algorithm.

#### Acknowledgments

The authors acknowledge support in part by the DoD Prostate Cancer Research Program (W81XWH-11-1-0232) and the National Institutes of Health (R01CA138662). The authors express sincere appreciation to ISS, Inc (Champaign, IL) for their persistent support and technical assistance over years of study. We also appreciate the assistance from Mr. Henry Tran who provided key literature search on the relationship between observed fluorescence signals and biochemical compounds of tissue as well as prostate cancer.